CHAPTER 6

VARIATIONAL METHOD FOR UNSATURATED SOIL SLOPES

6.1 INTRODUCTION AND REVIEW OF EXISTING STUDIES

The stability analyses in the previous chapters are carried out by implementing the conventional saturated soil mechanics. The soils are assumed to be either completely dry (S=0) or completely saturated (S=1); S represents degree of saturation. Terzaghi's (1943) effective and total stress is used to model the soil below (S=1) and above (S=0) the groundwater table. However, in reality, the soil above the groundwater table remains in a partially saturated state ($0<S<1$). The development of the negative pore-water pressure in the unsaturated medium enhances the overall strength and stiffness of the soil. Therefore, neglecting the effect of matric suction during the analysis of slopes eventually leads to an uneconomical design, especially, in arid and semi-arid zones, where the moisture loss due to evaporation is higher than the rainfall-induced infiltration. Unlike Terzaghi's effective stress parameter, which is the sole controlling parameter for predicting the engineering behaviour of saturated soil, two stress parameters are required to completely describe the stability and the deformational aspects of the partially saturated soil, namely, net normal stress and matric suction. Fredlund and Morgenstern (1977) were the pioneers to propose a modified Mohr-Coulomb yield criterion on the basis of these two stress state variables. By using this criterion, stability analyses were performed on homogeneous unsaturated slopes with the help of (a) limit equilibrium method (Fredlund and Rahardjo 1993; Lu and Godt 2008; Travis et al. 2010; Gavin and Xue 2010; Vahedifard et al. 2016), finite element method (Cho and Lee 2001, 2002; Cai and Ugai 2004; Griffiths and Lu 2005;

Hamdhan and Schweiger 2013), upper bound limit analysis with rigid block method (Sun et al. 2019), and finite difference code, FLAC (Sun et al. 2016; Kang et. al. 2020).

The literature review clearly reveals that most of the analytical works were carried out on the basis of conventional LEM, where the assumptions regarding the shape of the slip surface, normal stress along the slip surface, and interslice forces are required to consider prior to the analysis. The variational method, which is constructed on the working platform of LEM, is devoid of such statical and kinematical assumptions. However, researchers have never provided any closed-form solutions for estimating the stability of unsaturated soil slopes by employing calculus of variation. This creates an urge to carry out the present research. In the present work, the variational approach is applied to propose the closed-form critical factor of safety and to determine the corresponding critical slip surface of the homogeneous unsaturated soil slopes considering the fluctuations of the water table and the change in climatic conditions. The unsaturated soil above the water table is modelled by suction-stress-based effective stress approach; the expression of suction stress is obtained by incorporating the suitable soil water characteristics curve (SWCC) and hydraulic conductivity function (HCF). The stability charts are proposed for different combinations of slope angle, slope height, soil friction angle, air entry value, pore size spectrum number, flow conditions (evaporation (positive), precipitation (negative), and no-flow (zero flow)), and water table height. An attempt has also been made to analyze the stability of slopes subjected to unsteady (transient) flow.

6.2 PROBLEM STATEMENT AND CONSIDERED ASSUMPTIONS

The water table of a rectilinear homogeneous and isotropic cohesive-frictional soil slope, having slope angle β, is lying at a distance of h_w from the toe of the slope.

The schematic diagram of the problem is represented in Fig. 6.1. The soil below and above the water table is considered to be completely and partially saturated, respectively. The climatic change, the rise of sea level, and the increase in the intensity of precipitation directly or indirectly affect the degree of saturation in the unsaturated zone, leading to slope failure. With the help of variational technique, it is intended to locate the critical slip surface and the corresponding safety factor by duly considering the effect of seasonal changes which causes infiltration, evaporation, and thereby, water

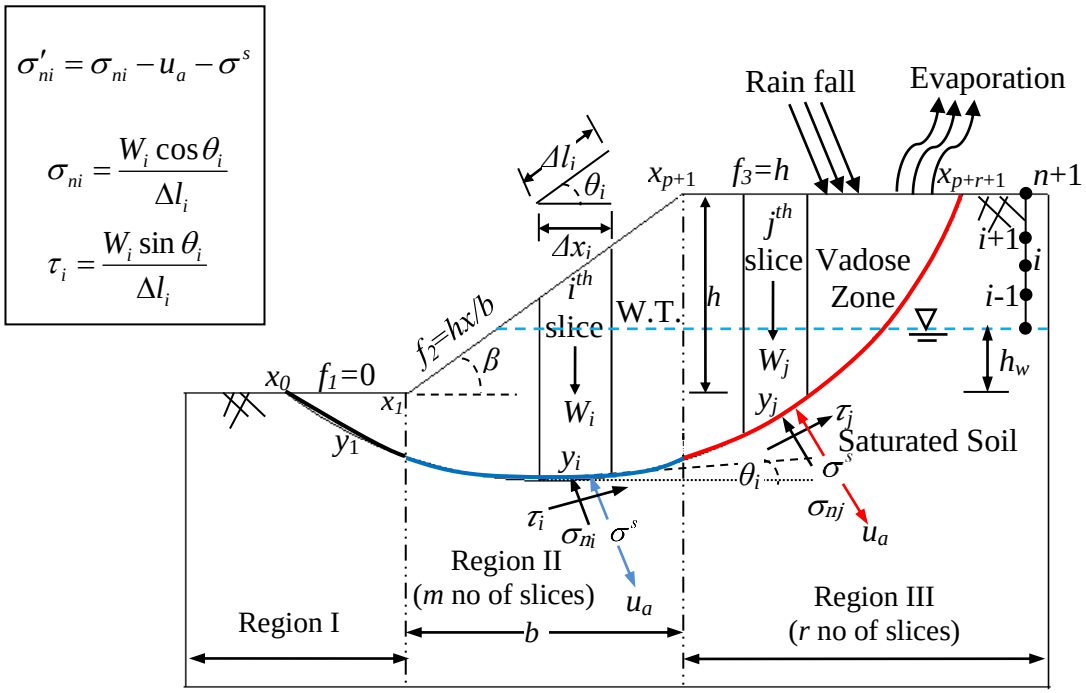

Fig. 6.1 Schematic representation of the chosen unsaturated soil slope of angle β along with the force distribution in two arbitrary slices.

table fluctuations within the soil medium. The fluid flow in the vadose zone is inviscid, irrotational, unidirectional (vertical), steady-state, transient, and governed by Darcy's linear flow law. The permeability in the vadose zone is modeled by Gardner's HCF (Gd-HCF). Most of the analyses consider the time-independence of the flux. However, the transient analysis is also carried out for a few cases. The failure of the soil is governed by the modified Mohr-Coulomb yield criterion (MMC) and the variation of

the suction stress in the unsaturated portion is taken care of by the employment of SWCC (van-Genuchten's SWCC (vG-SWCC), Gardner's SWCC (Gd-SWCC)) and suction stress characteristics curve (SSCC).

6.2.1 Suction-stress, vG-SWCC, Gd-SWCC, Gd-HCF, and MMC

In the early twenty-first century, Lu and Likos (2004, 2006) promulgated the suction stress-based unified effective stress formulation which is quite fundamental in nature and flexible in application. The suction stress is a stress state variable that considers all the physical interparticle stress mechanisms, such as physicochemical forces, surface tension, and capillarity forces in in the vadose zone. Lu and Likos (2004) categorically mentioned the benefits of suction stress in removing the limitations inherently associated with Bishop's (1959) effective stress parameter.

On the basis of the thermodynamic equilibrium principle, Lu et al. (2010) proposed the following relationship between suction stress and matric suction:

$$\sigma^s = -(u_a - u_w)\Theta_n = -(u_a - u_w)S_e \tag{6.1}$$

Here, (i) u_a–u_w defines the matric suction (ψ), i.e., the difference between the pore air (u_a) and pore water (u_w) pressures.

(ii) Θ_n and S_e denote the normalized volumetric water content and the effective degree of saturation, respectively. They are defined as:

$$\Theta_n = \frac{\theta - \theta_r}{\theta_s - \theta_r};\ S_e = \frac{S - S_r}{1 - S_r} \tag{6.2}$$

Corresponding to any matric suction, θ and S represent the volumetric water content and the degree of saturation, respectively. The subscripts '*s*' and '*r*' indicate the saturation and the residual state, respectively.

The three-parameter dependent van- Genuchten's (1980) soil water characteristics curve (SWCC) is adopted here to model the Θ_n- ψ relationship in the vadose zone

under steady-state flow. The reason for choosing van-Genuchten (vG) model over the other SWCC model is its simplicity, invertibility, and smoothness. Mathematically, vG-SWCC model is expressed as:

$$\Theta_n = \left\{ \frac{1}{1+(\alpha\psi)^n} \right\}^m \tag{6.3}$$

The mathematical parameters α, n, and m can be attributed to the physical characteristics of the soil; α is related with the air entry value (AEV), n represents the pore size distribution, and m controls the sigmoidal shape of the SWCC curve. Coarse-grained soils are customarily associated with high α (can be at the extent of 1-2 kPa^{-1}), whereas lower values of α (can be as low as 0.0005 kPa^{-1}) typically correspond to fine-grained soils. The magnitude of n generally varies within a certain limit of 1.1-8.5 (Lu and Likos 2004); larger values of n replicate the soil having a relatively uniform pore size distribution. Considering the easiness in obtaining the analytical solutions, m is taken to be equal to (1-1/n) in most of the literature. In the present analysis, following Mualem's hydraulic conductivity model, m is assumed to be related to n through the following expressions:

$$R_M = m - 1 + 1/n \tag{6.4}$$

Combining Eqs. (6.1) and (6.3) the following closed-form expression (Lu et al. 2010) of suction stress characteristics curve (SSCC) is obtained for all soils having variably saturation state.

$$\sigma^s = -(u_a - u_w) \qquad u_a\text{-}u_w \le 0 \tag{6.5a}$$

$$= -(u_a - u_w)\left\{ \frac{1}{1+\left[\alpha(u_a - u_w)\right]^n} \right\}^m \qquad u_a\text{-}u_w \ge 0 \tag{6.5b}$$

Following a few literature (Yeh 1989; Srivastava and Yeh 1991; Lu and Likos 2004; Lu and Godt 2013; Shahrokhabadi et al. 2019), Gardner's SWCC (1958) model abbreviated as Gd-SWCC model, a simple and widely used functional form (Eq. 6.6), is employed herein to accommodate the transient analysis:

$$\Theta_n = \frac{\theta - \theta_r}{\theta_s - \theta_r} = \exp\left[-\alpha\left(u_a - u_w\right)\right] \tag{6.6}$$

The variation of the volumetric water content can, therefore, be written as:

$$\theta = \theta_r + (\theta_s - \theta_r)\exp\left[-\alpha\left(u_a - u_w\right)\right] \tag{6.7}$$

The Gd-SWCC parameter α, in a very rudimentary sense, shows the inverse of the air entry value, which is defined as the matric suction at which air starts entering the soil medium and becomes a continuous phase. The impacts of θ_s, θ_r, and α on the Gd-SWCC drying profiles are displayed in Fig. 6.2a. For the purpose of illustration, two values are chosen for each of these parameters. The boundary effect zone becomes narrower with the increase in α. The desaturation rate seems to be influenced by the saturated- and residual state volumetric water content. The variations of normalized (Θ_n) and dimensionless (Θ_d) volumetric water content are presented in Fig. 6.2b. Unlike the Θ_n curves, which remain solely dependent on α, the form of the Θ_d curves gets dictated by α, θ_s and θ_r.

Following Gardner's SWCC (1958) model, the suction stress can be expressed in an alternative form:

$$\sigma^s = -\left(u_a - u_w\right) \qquad u_a\text{-}u_w \le 0 \tag{6.8a}$$

$$= \left(u_a - u_w\right)\exp\left[-\alpha\left(u_a - u_w\right)\right] \qquad u_a\text{-}u_w \ge 0 \tag{6.8b}$$

Due to the variation in the water content, the pore water flow rate no longer remains constant in the vadose zone. The Gd-HCF model ($k = k_s \exp\left(-\alpha\psi\right)$; k_s =

saturated hydraulic conductivity) captures the influence of matric suction on the variation of the hydraulic conductivity above the GWT. The influence of k_s, and α on the HCF and the relative permeability (non-dimensional) profiles are shown in Figs. 6.2c and 6.2d. It is to be noted that both the models (Gd-SWCC and Gd-HCF) are independent of the desaturation rate.

The stability of slope is assessed by duly modifying the linear Mohr-Coulomb failure criterion (MMC) which takes into account the effect of suction stress (σ^s) apart from the saturated strength parameters, namely, the effective cohesion (c'), and the effective friction (ϕ'). The basis of this modification lies in the following unified effective stress formulation as prescribed by Lu and Likos (2004):

$$\underset{\text{Effective Stress}}{\sigma'} = \underset{\text{Net normal Stress}}{(\sigma - u_a)} - \underset{\text{Suction Stress}}{\sigma^s} \quad ; \quad u_a = \text{pore air pressure} \tag{6.9a}$$

$$\text{MMC:} \quad \tau_t = c' + \sigma' \tan\phi' \quad \Rightarrow \quad \tau_f = c' - \sigma^s \tan\phi' + (\sigma - u_a)\tan\phi' \tag{6.9b}$$

$$\Rightarrow \quad \tau_f = c' + c'_{apparent} + (\sigma - u_a)\tan\phi' \tag{6.9c}$$

where, $c'_{apparent} = -\sigma^s \tan\phi'$

The modified Mohr-Coulomb equation for unsaturated soils, as represented by Eqs. (6.9b), (6.9c), features the additional effect of apparent cohesion ($c'_{apparent}$). Due to the variation in suction stress, the Mohr yield circle and Mohr yield envelope becomes spatially dependent along the vertical axis. With the increase in suction stress, the Mohr yield circle grows in size and the Mohr yield envelope shifts parallelly based on the magnitude of $c'_{apparent}$, as depicted in Fig. 6.3.

The suction stress replaces the matric suction in the conventional three-dimensional stress space. The advantage of reframing the stress state variable is that the curvilinear form of the three-dimensional failure planes gets converted into the planar one, as pictorially represented in Fig. 6.4a. This conversion is due to the fact that,

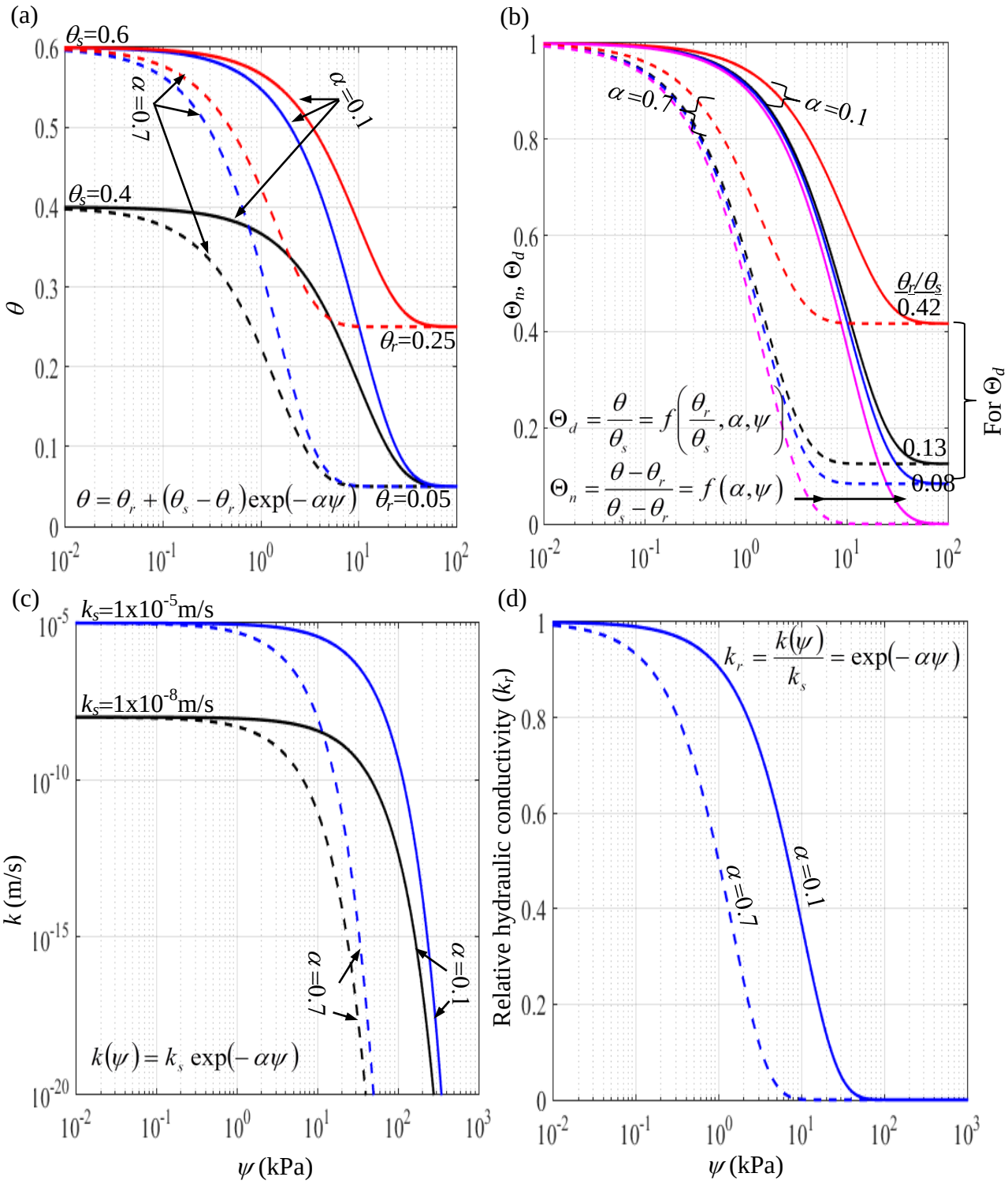

Fig. 6.2 Impact of air entry value, saturation state, and the residual state on the (a) $\theta-\psi$, (b) Θ_n (Θ_d) $-\psi$, (c) $k-\psi$, and (d) $k_r-\psi$.

unlike the $\tau - \psi$ plane, the strength parameter (ϕ^b) in the $\tau - \sigma^s$ plane becomes constant. Fig. 6.4b shows the schematic diagram of the failure plane in two-dimensional stress spaces ($\tau - \psi$ and $\tau - \sigma^s$ planes). In case of the transient flow, due to the tempo-spatial

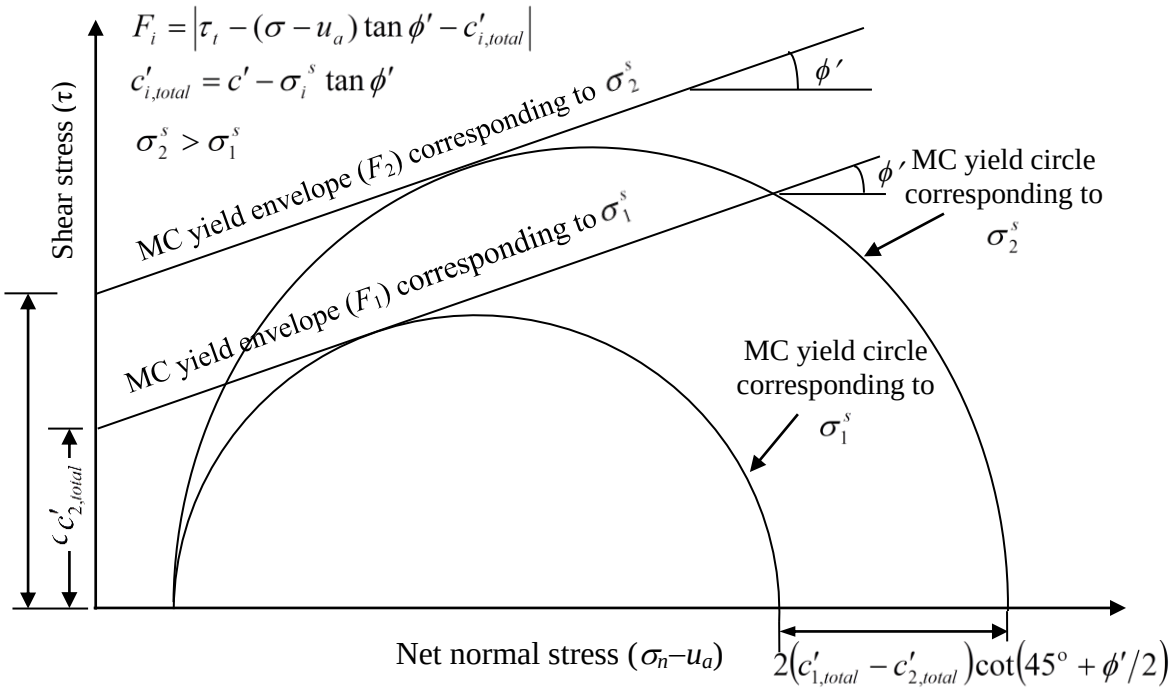

Fig. 6.3 Effect of suction stress on the structure of MC yield envelope and MC yield surface.

variation of suction stress, the failure envelope above the GWT not only depends on the spatial point but also gets influenced by the temporal component.

6.2.2 Steady-State Flow

Adopting Darcy's flow law and Gardner's (1958) one parameter hydraulic conductivity function (HCF), the matric suction (ψ) of unsaturated soil subjected to steady-state flow condition (i.e. the net flow through any element at a fixed point in space is zero and independent of time) can be represented as a function of depth above the water table (z).

$$\Rightarrow \psi = -\frac{1}{\alpha}\ln\left[(1+Q)\exp(-\alpha\gamma_w z) - Q\right] \tag{6.10}$$

Substituting the expression of matric suction (as describe in Appendix A.1) into Eqs. (6.5a) and (6.5b), the suction stress in non-dimensional form can be rewritten as follows:

$$\alpha\sigma^s = \frac{\ln\left[(1+Q)\exp(-\alpha\gamma_w z) - Q\right]}{\left(1+\left\{-\ln\left[(1+Q)\exp(-\alpha\gamma_w z) - Q\right]\right\}^n\right)^m} \tag{6.11}$$

In Eq. (6.11) (Lu and Likos 2004), the terms $\alpha\sigma^s$, $\gamma_w\alpha z$, and Q (=q/k_s) are the dimensionless parameters pertain to suction stress, depth, and flow ratio. The hysteresis in the drying and the wetting SWCC paths can be well considered in the present formulation by considering different values of α; nevertheless, the parameter n is almost indifferent to the flow direction.

Figs. 6.5a-6.5d demonstrates the variation of suction stress in the vertical direction above the water table corresponding to different steady-flow, and various α and R_M parameters. When the infiltration rate equals the saturated permeability (i.e. $q = -k_s$), the suction stress becomes zero throughout the depth. Irrespective of R_M, the suction stress profiles for various flow rates are quite distinct when α=0.01, whereas, the suction stress profiles coincide with each other for $\alpha \geq 0.1$. Nevertheless, the R_M parameter significantly impacts the magnitude of the suction stress as well as the trend of the suction stress profiles. The higher the R_M lower is the effective stress. Corresponding to R_M =2, the curves manifest peak suction stress especially, for the evaporative condition. Conversely, no peak point seems to exist for R_M =0 and α=0.01. Another notable observation for lower AEV is that when R_M increases, the zone above the water table at which suction stress remains to be considerable reduces to a great

extent. The impact of the R_M values on the suction stress profiles shows the relevance of the independence of the m parameter.

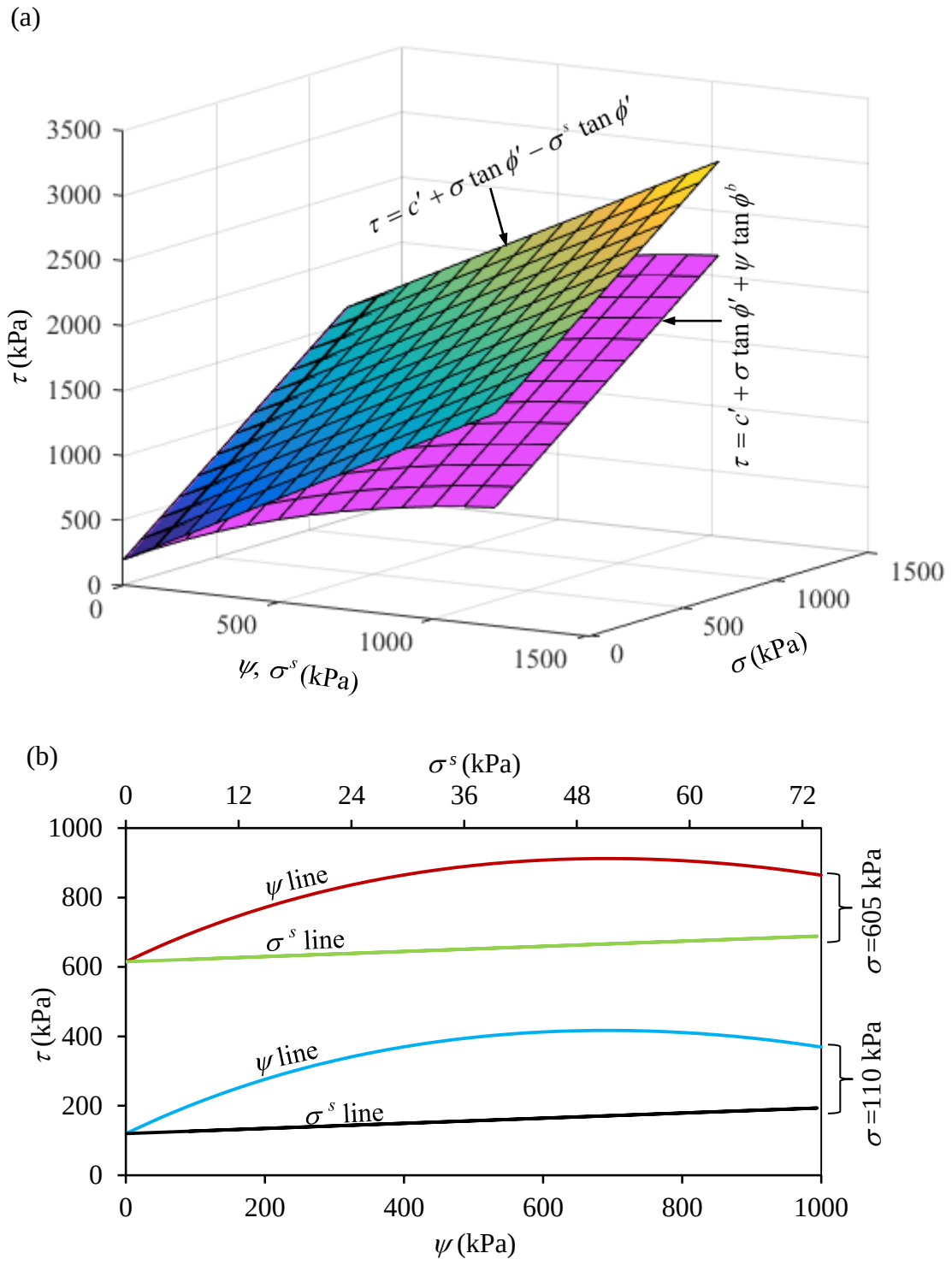

Fig. 6.4 The shear strength failure envelope in different (a) three-dimensional stress spaces, namely, $\tau - \psi - \sigma$ and $\tau - \sigma^s - \sigma$, and (b) two-dimensional stress planes, namely, $\tau - \psi$ and $\tau - \sigma^s$.

By substituting the expression of matric suction ($\psi = u_a$-u_w) into Eqs. (6.8a) and (6.8b), the suction stress obtained from Gardner's SWCC model (1958) can be expressed in a non-dimensional form:

$$\alpha\sigma^s = \left[(1+Q)\exp(-\alpha\gamma_w z) - Q\right]\ln\left[(1+Q)\exp(-\alpha\gamma_w z) - Q\right] \tag{6.12}$$

Fig. 6.6 depicts the variation of the suction stress profiles obtained by the use of vG and Gardner's SWCC model and subjected to various infiltration rates. At any spatial position subjected to a specific Q (q/k_s), vG-SWCC model appears to predict a higher amount of suction stress than the Gardner's SWCC model. The band-gap of the suction stress profiles, near the ground surface, is significantly wider when vG-SWCC model is employed. This gives an impression that the suction stress, and consequently, the soil slope stability will get relatively less influenced by the Gardner's SWCC model.

6.2.3 Transient State Flow

The suction stress is obtained by numerically solving the widely used Richards' equation (1931), which models the unidirectional transient flow of pore water in unsaturated homogeneous and isotropic soil.

$$\frac{\partial}{\partial z}\left[k(h_m)\left(\frac{\partial h_m}{\partial z}+1\right)\right] = \frac{\partial\theta}{\partial t} \tag{6.13}$$

here, (i) $h_m(z,t)$ represents depth (z)- and time (t)-dependent matric suction head. Mathematically, $h_m = \psi/\gamma_w$.

(ii) $k(h_m)$ and $\theta(h_m)$ are the h_m-dependent functionals that are controlled by Gd- HCF and Gd-SWCC models, respectively. Plugging the expressions of $k(h_m)$ and $\theta(h_m)$ into Eq. (6.13), the following nonlinear parabolic partial differential equation is obtained (as shown in Appendix A.2) with certain constraints.

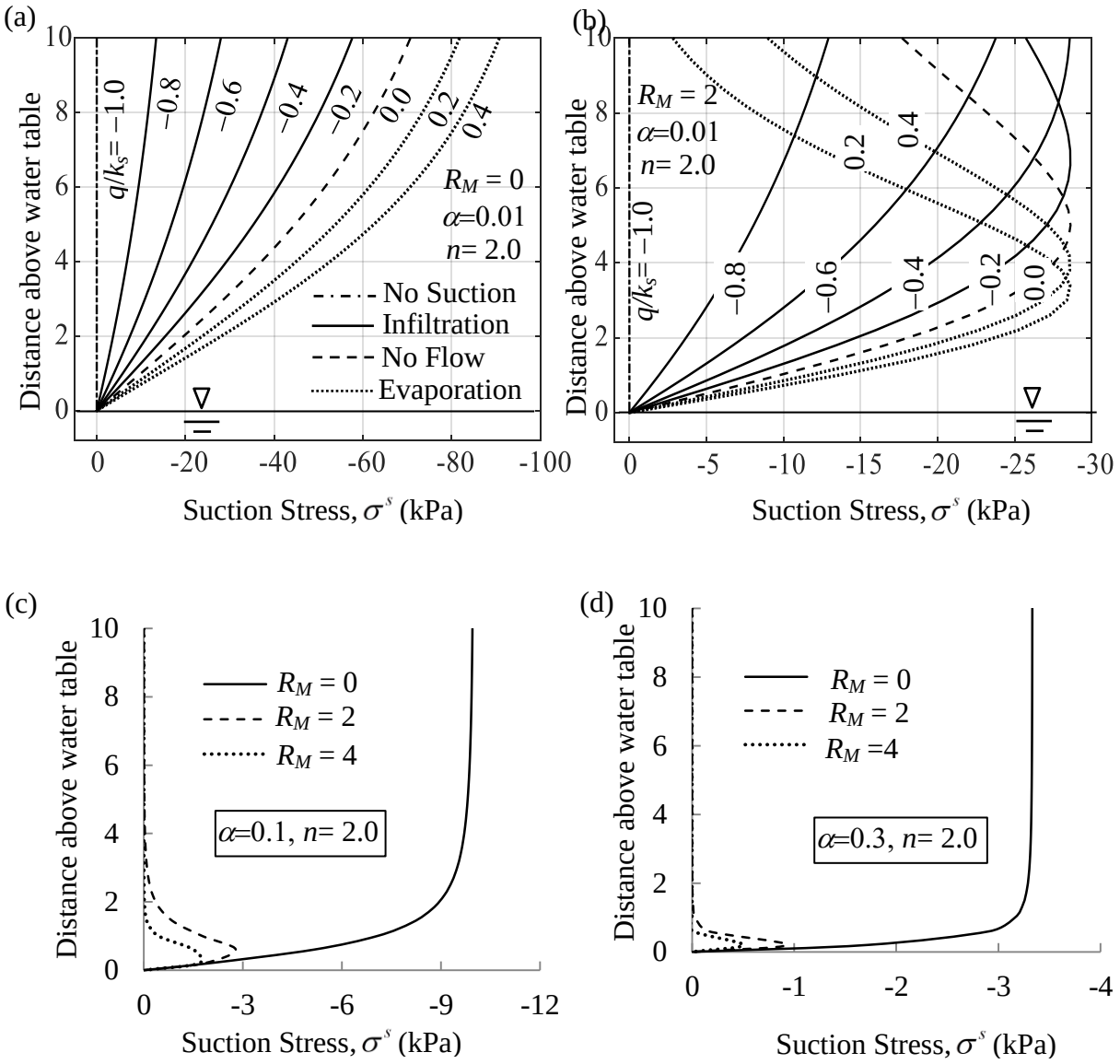

Fig. 6.5 The variation of σ^s with the distance above water table (z) corresponding to (a-d) steady state flow with different values of α :(a-b) α = 0.01 kPa^{-1}, (c) α = 0.1 kPa^{-1}, and (d) α = 0.3 kPa^{-1}.

Governing Differential Equation:

GD SWCC:
$$\left[\frac{\partial^2 h_m}{\partial z^2} + \alpha\left(\frac{\partial h_m}{\partial z}\right)^2\right] + \alpha\frac{\partial h_m}{\partial z} = \lambda\frac{\partial h_m}{\partial t} \tag{6.14a}$$

vG SWCC:
$$\left[\frac{\partial^2 h_m}{\partial z^2} + \alpha\left(\frac{\partial h_m}{\partial z}\right)^2\right] + \alpha\frac{\partial h_m}{\partial z} = \lambda\frac{\partial h_m}{\partial t} \tag{6.14b}$$

Subjected to: (a)Initial conditions: $h_m(z,0)= -z$ (6.15a)

(b)Boundary conditions (BCs):

(i) Head (Dirichlet) BC @ GWT: $h_m(0, t)=0$ (6.15b)

(ii) Flux (Neumann) BC @GS: $\left[k(h_m)\left(\frac{\partial h_m}{\partial z}+1\right)\right]_{z=h} = q$ (6.15c)

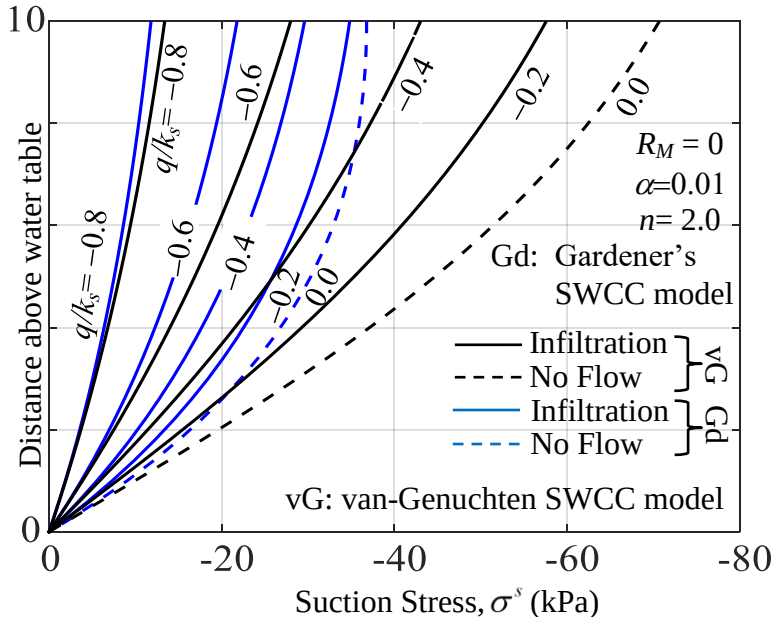

Fig. 6.6 The σ^s profiles obtained from vG and Gardner's SWCC model corresponding to various infiltration rates.

where, $\lambda = \frac{\alpha(\theta_s-\theta_r)}{k_s} = \lambda^{Gd}$ Gardner's SWCC

$= -\frac{mn\alpha(\theta_s-\theta_r)(\alpha h_m)^{n-1}}{k_s \exp(\alpha h_m)\{1+[\alpha h_m]^n\}^{m+1}} = \lambda^{vG}$ vG - SWCC

This initial value problem (IVP) is solved with the aid of the Crank-Nicolson finite difference implicit (CN-FDM) technique. This method is unconditionally stable and provides 2nd order convergence in time as well as space. To avoid the complexities associated with nonlinearity, the square of the first-order derivative term and λ^{vG} in the governing equation are evaluated in the previous (known) time step. The detailed

numerical formulations are mentioned in Appendix A.3. The spatial discretization of the domain is shown in Fig. 6.1. Except for the two extremities, Eqs. (6.14a) and (6.14b) must be satisfied in all the nodes. The obtained simultaneous sets of linear equations ($\boldsymbol{A}\boldsymbol{H}_m^{t+\Delta t} = \boldsymbol{B}^t$) are solved through the Gauss elimination technique. To avoid any spurious oscillations, the depth (Δz)- and the time (Δt)-increments are chosen to be small enough so that the non-dimensional terms, m_1, and m_2, as mentioned in Appendix A.3, should not be very high. Unlike silt and clay, a strict restriction requires to be maintained on the values of m_1 and m_2 for sandy soils. The possible combinations of m_1 and m_2 are shown in Fig. 6.7, corresponding to various θ_s, θ_r, and α. Any combination chosen outside these envelopes will yield an imaginary solution. The permissible time increments (Δt) are further tabulated and presented in Table 6.1; Δt reduces with the increase in α and θ_r, and decrease in θ_s. With forward time-marching, the coefficient matrix A remains unchanging, and the unknown variable vectors ($\boldsymbol{H}_m^{t+\Delta t}$) and right-hand side vectors ($\boldsymbol{B}^t$) are updated accordingly. The obtained h_m will eventually provide the effective stress that will be used in computing the stability of the slopes. In Fig. 6.8, the σ^s profiles above the water table are plotted after various durations, namely, 10, 50, 100, 200, 300, 400, 1000, 40000, and 100000 days. It can be observed that as time progresses, the transient profiles approach the steady-state curve.

Table 6.1 The permissible time increment to obtain real values of m_1 and m_2 coefficient for sand (k_s= 5.0 x 10^{-6} m/s).

α (m^{-1})	Permissible Time element Δt (in seconds)		
	θ_s=0.41; θ_r=0.05	θ_s=0.38; θ_r=0.05	θ_s=0.38; θ_r=0.01
0.6	1281	996.5	1117.2
0.7	560	469	526
0.8	301	246	276.6
0.9	190	131	147
1.0	132	71	80

6.3 FORMULATIONS

In this chapter, the variational formulation has been further extended to evaluate the stability of the unsaturated soil slopes made of cohesive-frictional material. Based on the ordinary method of slices, the factor of safety is computed through the following expression:

$$F = \frac{\text{Available Resisting Moment}}{\text{Actual Driving Moment}} = \frac{\sum_{i=1}^{n} \tau_f}{\sum_{i=1}^{n} \tau_i} = \frac{\sum_{i=1}^{n} \left[c' + \sigma'_{ni} \tan \phi' \right]}{\sum_{i=1}^{n} \tau_i}$$
$$= \frac{\sum_{i=1}^{n} \left[c' \Delta l_i + \left(W_i \cos \theta_i - u_a \Delta l_i - \sigma^s_{avg,i} \Delta l_i \right) \tan \phi' \right]}{\sum_{i=1}^{n} W_i \sin \theta_i} \tag{6.16}$$

This expression is obtained by satisfying the static equilibrium condition along the horizontal and vertical axes. In this expression, (i) θ_i, Δx_i, Δl_i (=$\Delta x_i/\cos\theta_i$), W_i and $\sigma^s_{avg,i}$ are the inclination angle, width, length, weight, and average suction stress of any arbitrary i^{th} slice, respectively, as shown in Fig. 6.1, and (ii) n represents the total number of slices.

For most of the unsaturated problems encountered in the field, pore air pressure (u_a) is assumed to be the same as atmospheric pressure (Vahedifard et al. 2016; Sun et al. 2019) which eventually implies u_a=0. Eq. (6.16) can, therefore, be rewritten as the following form:

$$F = \frac{\sum_{i=1}^{n} \left[c' \Delta x_i \sec^2 \theta_i + \left(W_i - \sigma^s_{avg,i} \Delta x_i \sec^2 \theta_i \right) \tan \phi' \right]}{\sum_{i=1}^{n} W_i \tan \theta_i} \tag{6.17}$$

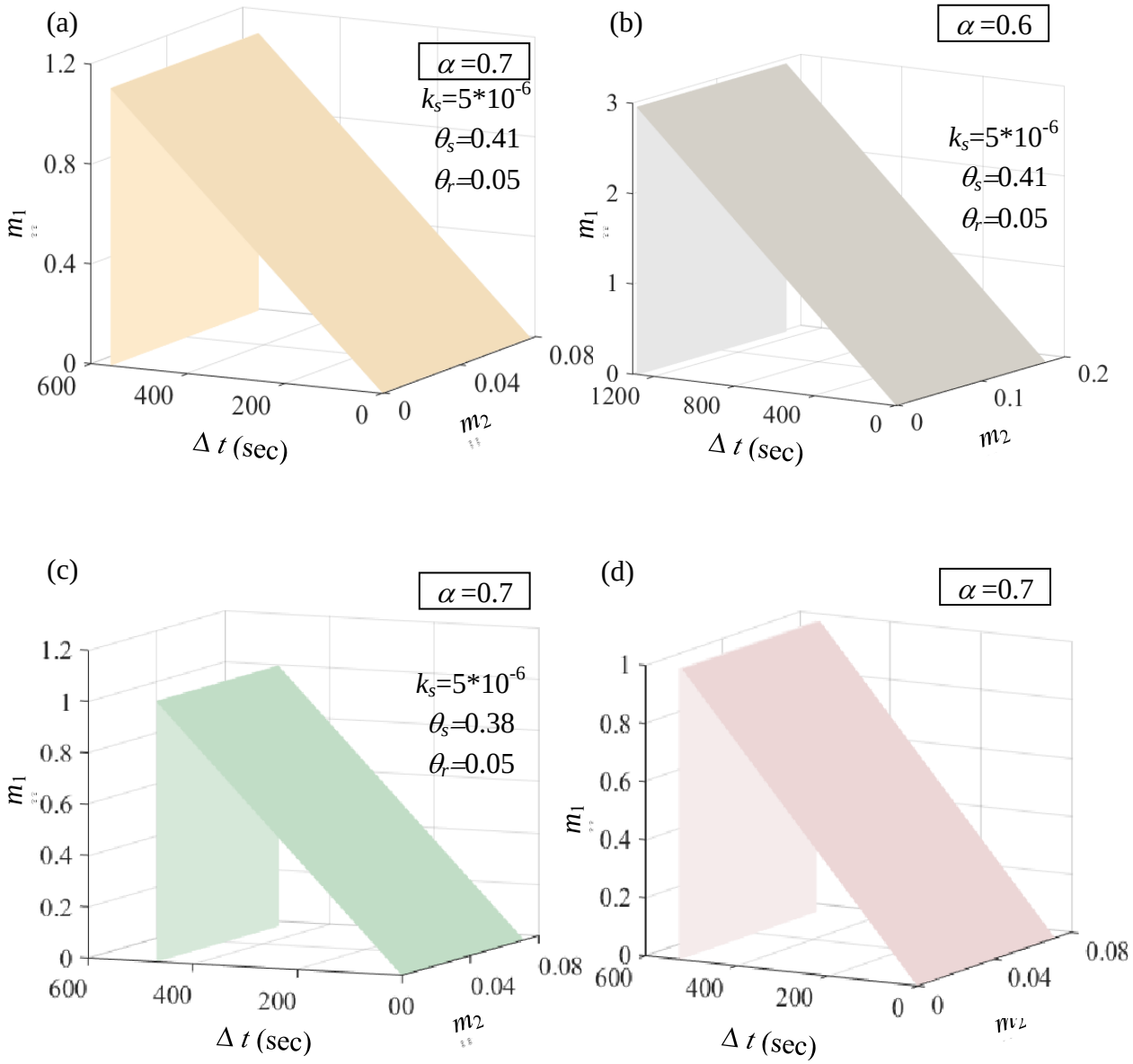

Fig. 6.7 Limiting envelopes of m_1, m_2 with respect to Δt for sand.

In adherence to the research work of Revilla and Castillo (1977) and Baker and Garber (1978), the discrete analytical formulation written in Eq. (6.17) can be further expressed as the following continuous form along the slip surface.

$$F = \frac{\int_{x_0}^{x_n} \left[c'\left(1+y_i'^2\right) + \left\{ \gamma\left(f_i - y_i\right) - \sigma_{avg,i}^{s}\left(1+y_i'^2\right) \right\} \tan\phi' \right] dx}{\int_{x_0}^{x_n} \left[\gamma\left(f_i - y_i\right) y_i' \right] dx} = \frac{\int_{x_0}^{x_n} Q_i\left(x, y, y'\right) dx}{\int_{x_0}^{x_n} R_i\left(x, y, y'\right) dx} \qquad (6.18)$$

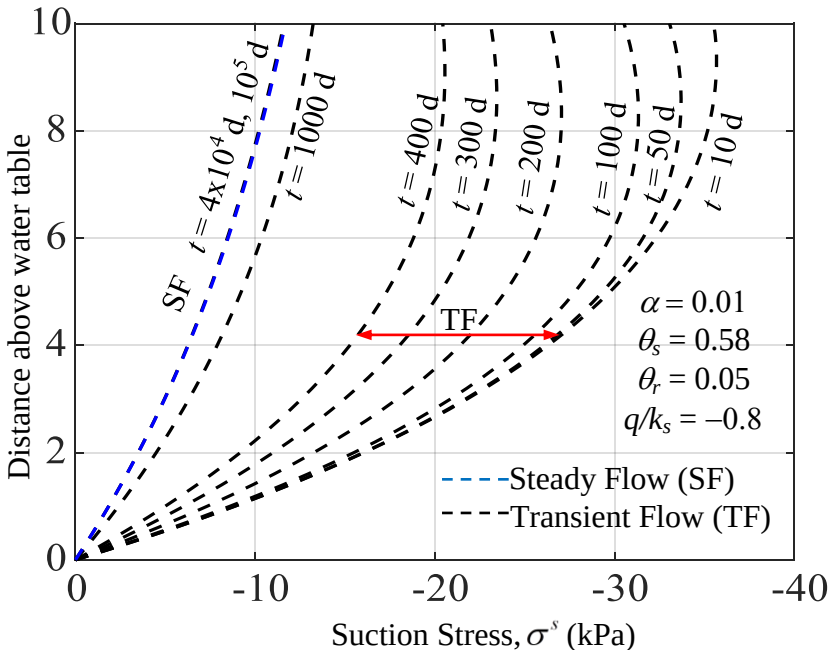

Fig. 6.8 The variation of σ^s with the distance above water table (z) corresponding to transient flow.

where, (i) x_0 and x_n are the abscissa of the start and the end-points of the slip surface, respectively;

(ii) $y_i' = \tan\theta_i$;

(iii) $W_i = \gamma (f_i - y_i)\Delta x_i$; γ is the unit weight of unsaturated soil and f_i and y_i indicate the slope and slip surface associated with i^{th} slice, respectively. The expression of f_i corresponding to each region can be represented as the following mathematical form:

$$\text{Region I: } f_I(x) = 0; \qquad x_0 \le x \le 0 \tag{6.19a}$$

$$\text{Region II: } f_{II}(x) = hx/h_1; \quad 0 \le x \le h_1 \tag{6.19b}$$

$$\text{Region III: } f_{III}(x) = 0; \qquad h_1 \le x \le x_n \tag{6.19c}$$

Both Q_i's and R_i's are the function of slip surface, slope surface, and the normal stresses acting on the slip surface and hence, they are functionals. The critical factor of safety (F_s) is obtained by optimizing these functionals with the aid of Euler–Lagrangian equation, as suggested in the calculus of variation.

$$F_s = \frac{\dfrac{\partial Q_i}{\partial y_i} - \dfrac{d}{dx}\left(\dfrac{\partial Q_i}{\partial y_i'}\right)}{\dfrac{\partial R_i}{\partial y_i} - \dfrac{d}{dx}\left(\dfrac{\partial R_i}{\partial y_i'}\right)} = \frac{\gamma \tan\phi' + 2c'y_i'' - 2y_i''\sigma^s_{avg,i}\tan\phi'}{\gamma f_i'} \tag{6.20}$$

By integrating Eq. (6.20), the expression of slip surface in each distinct region can be represented as follows:

$$y_i = P_i x^2 + B_i x + D_i \quad (i = 1, 2, 3, \ldots\ldots, n, \text{ refers to the slice nos.}) \tag{6.21}$$

Here, (i) the expression of coefficient P_i 's are as follows:

$$P_i = -\frac{\gamma \tan\phi'}{4\left(c' - \sigma^s_{avg,i}\tan\phi'\right)} \quad \text{(Region I and III)} \tag{6.22a}$$

$$P_i = -\frac{1}{4\left(c' - \sigma^s_{avg,i}\tan\phi'\right)}\left(\gamma \tan\phi' + \frac{c'}{Nh_1}\right) \quad \text{(Region II)} \tag{6.22b}$$

N (= $c'/F_s\,\gamma h$) defines the non-dimensional stability number. (6.22c)

(ii) The expression of the unknown integrating constants B_i's and D_i's, associated with the corresponding slip surface of each slice, are obtained by solving a consistent set of linear and non-linear equality constraints as mentioned in Section 3.3.6. The available known equations are (a) 2 transversality conditions, (b) n number of continuity equations, (c) n number of natural boundary conditions, and (d) one equation concerning the factor of safety. Hence, the total number of available equations ($2n$ + 3) are exactly equal to the total number of unknown variables comprises of (a) two end points (x_0 and x_n), (b) $2n$ number of integrating constants (B_1, B_2, …….., B_n, D_1, D_2,……, D_n), and (c) one critical factor of safety (F_s). Moreover, the system of equations is independent in nature. Hence, a unique solution is obtained. In the present work, in accordance with Vahedifard et al. (2016), Sun et al. (2019), the homogenous unsaturated soil slope is assumed to fail by the development of toe failure surface (i.e. x_0 = 0). Consequently, Region I can be disregarded without further consideration. To

obtain a generalized expression of the coefficients, Regions II and III are first divided into limited number of slices, (such as, 2, 3, 4 etc.) and the expressions of the coefficients are obtained by hand-calculations. They are presented in Tables 6.2-6.4. This exercise is carried out by taking a few additional numbers of slices and the derived coefficients are then closely scrutinized. A very well-defined pattern is attained in the coefficient formulations. Table 6.5 illustrates the form of B_i and D_i for any arbitrary number of finite divisions in Regions II and III along with the expression of N_i.

6.4 ANALYSIS TECHNIQUES

The methodology conceived in the present work is iterative in nature. The step wise procedure is mentioned in the following steps.

Step I: Plug all the input (material, geometrical, flow characteristics, water table depth) parameters.

Step II: Divide the Regions II and III into *m* and *r* number of horizontal and vertical slices respectively.

Step III: Construct the slip surface and evaluate the corresponding critical F_s and N value by using the expressions mentioned in the previous section. For the first iteration suction stress above the water table is neglected (i.e. $\sigma^s = 0$).

Step IV: Evaluate the magnitude of suction stress at the central point of each segment above the water table and compute the weighted average of suction stress for each slice ($\sigma^s_{avg,i}$).

Step V: Go to **Step III** and repeat the process of slip surface construction and critical factor of safety evaluation until the previous and the current iteration provides the same solution. Mathematically, three stopping criteria are specified to capture the solution:

Table 6.2 The expression of B_i's and D_i's by considering two and three slices in Region II.

m=2, r=1	m=3, r=1
$B_1 = B_2 = -1$	$B_1 = B_2 = -1$
$B_3 = \frac{Th_1}{4}(A_2 - A_1) + \frac{c'}{4N}(A_1 - A_2) - 1$	$B_3 = \frac{Th_1}{6}(A_2 - A_1) + \frac{c'}{6N}(A_2 - 2A_3 + A_1) - 1$
$B_4 = 1 + \frac{TA_3 x_4}{2}$	$B_5 = 1 + \frac{TA_4 x_5}{2}$
$D_1 = D_2 = 0$	$D_1 = D_2 = 0$
$D_3 = -\frac{Th_1^2}{16}(A_2 - A_1) - \frac{c'h_1}{16N}(A_1 - A_2)$	$D_3 = -\frac{Th_1^2}{36}(A_2 - A_1) - \frac{c'h_1}{36N}(A_1 - A_2)$
$D_4 = \frac{Th_1^2}{16}(4A_3 - 3A_1 - A_2) + \frac{c'h_1}{16N}(A_2 + 3A_1)$ $-2h_1 - \frac{TA_3 x_4 h_1}{2}$	$D_4 = \frac{Th_1^2}{9}(A_2 - A_3) + \frac{Th_1^2}{36}(A_1 - A_2) + \frac{c'h_1}{9N}(A_3 - A_2) + \frac{c'h_1}{36N}(A_2 - A_1)$
	$D_5 = \frac{Th_1^2}{36}(9A_4 - A_3 - 3A_2 - 5A_1) + \frac{c'h_1}{36N} + (3A_2 + A_3 + 5A_1) -$ $2h_1 - \frac{TA_4 x_5 h_1}{2}$
$N = \frac{c'(A_2 + A_1)}{4\left[2 + \frac{TA_3 x_4}{2} - \frac{Th_1(A_3 - A_2)}{2} - \frac{Th_1(A_2 - A_1)}{4}\right]}$	$N = \frac{c'(A_2 + A_3 + A_1)}{6\left[2 + \frac{TA_4 x_5}{2} - \frac{Th_1}{2}(A_4 - A_3) - \frac{Th_1}{6}(2A_3 - A_2 - A_1)\right]}$

Table 6.3 The expression of B_i's and D_i's by considering four and five slices in Region II.

m=4, r=1	m=5, r=1
$B_1 = B_2 = -1;\ B_3 = \frac{Th_1}{8}(A_2 - A_1) + \frac{c'}{8N}(A_1 - A_2) - 1$	$B_1 = B_2 = -1;\ B_3 = \frac{Th_1}{10}(A_2 - A_1) + \frac{c'}{10N}(A_1 - A_2) - 1$
$B_4 = \frac{Th_1}{8}(2A_3 - A_2 - A_1) + \frac{c'}{8N}(A_2 - 2A_3 + A_1) - 1$	$B_4 = \frac{Th_1}{10}(2A_3 - A_2 - A_1) + \frac{c'}{10N}(A_2 - 2A_3 + A_1) - 1$
$B_5 = \frac{Th_1}{8}(3A_4 - A_3 - A_2 - A_1) + \frac{c'}{8N}(A_3 - 3A_4 + A_2 + A_1) - 1$	$B_5 = \frac{Th_1}{10}(3A_4 - A_3 - A_2 - A_1) + \frac{c'}{10N}(A_3 - 3A_4 + A_2 + A_1) - 1$
$B_6 = 1 + \frac{TA_5}{2}x_6$	$B_6 = \frac{Th_1}{10}(4A_5 - A_4 - A_3 - A_2 - A_1) + \frac{c'}{10N}(A_4 - 4A_5 + A_3 + A_3 + A_1) - 1$
$D_1 = D_2 = 0;\ D_3 = -\frac{Th_1^2}{64}(A_2 - A_1) - \frac{c'h_1}{64N}(A_1 - A_2)$	$B_7 = 1 + \frac{TA_6}{2}x_7$, $D_1 = D_2 = 0;\ D_3 = -\frac{Th_1^2}{100}(A_2 - A_1) - \frac{c'h_1}{100N}(A_1 - A_2)$
$D_4 = \frac{Th_1^2}{16}(A_2 - A_3) + \frac{Th_1^2}{64}(A_1 - A_2) + \frac{c'h_1}{16N}(A_3 - A_2)$	$D_4 = \frac{Th_1^2}{25}(A_2 - A_3) + \frac{Th_1^2}{100}(A_1 - A_2) + \frac{c'h_1}{25N}(A_3 - A_2) + \frac{c'h_1}{100N}(A_2 - A_1)$
$+ \frac{c'h_1}{64N}(A_2 - A_1)$	$D_5 = \frac{Th_1^2}{100}(-9A_4 + 5A_3 + 3A_2 + A_1) + \frac{c'h_1}{100N}(9A_4 - 5A_3 - 3A_2)$
$D_5 = \frac{Th_1^2}{64}(-9A_4 + 5A_3 + 3A_2 + A_1) +$	$D_6 = \frac{Th_1^2}{100}(-16A_5 + 7A_4 + 5A_3 + 3A_2 + A_1) +$
$\frac{c'h_1}{64N} + (9A_4 - 5A_3 - 3A_2)$	$\frac{c'h_1}{100N}(16A_5 - 7A_4 - 5A_3 - 3A_2 - A_1)$
$D_6 = \frac{Th_1^2}{64}(16A_5 - A_4 - 3A_3 - 5A_2 - 7A_1) + \frac{c'h_1}{64N}$	$D_7 = \frac{Th_1^2}{100}(25A_6 - A_5 - 3A_4 - 5A_3 - 7A_2 - 9A_1) +$
$(A_4 + 3A_3 + 5A_2 + 7A_1) - 2h_1 - \frac{TA_5h_1}{2}x_6$	$\frac{c'h_1}{100N}(A_5 + 3A_4 + 5A_3 + 7A_2 + 9A_1) - 2h_1 - \frac{TA_6h_1}{2}x_7$
$N = \frac{c'(A_4 + A_3 + A_2 + A_1)}{8\left[2 + \frac{TA_5x_6}{2} - \frac{Th_1}{2}(A_5 - A_4) - \frac{Th_1}{8}(3A_4 - A_3 - A_2 - A_1)\right]}$	$N = \frac{c'(A_5 + A_4 + A_3 + A_2 + A_1)}{10\left[2 + \frac{TA_6x_7}{2} - \frac{Th_1}{2}(A_6 - A_5) - \frac{Th_1}{10}(4A_5 - A_4 - A_3 - A_2 - A_1)\right]}$

Table 6.4 The expression of B_i's and D_i's by dividing Region II and Region III both with two and three number of slices.

m=2, r=2	m=3, r=3
$B_1 = B_2 = -1;$ $B_3 = \frac{Th_1}{4}(A_2 - A_1) + \frac{c'}{4N}(A_1 - A_2) - 1$ $B_4 = \frac{Th_1}{4}(2A_3 - A_2 - A_1) + \frac{c'}{4N}(A_1 - A_2) - 1$ $B_5 = 1 + \frac{TA_4 x_5}{2}$, $D_1 = D_2 = 0$ $D_3 = -\frac{Th_1^2}{16}(A_2 - A_1) - \frac{c'h_1}{16N}(A_1 - A_2)$ $D_4 = \frac{Th_1^2}{4}(A_2 - A_3) + \frac{Th_1^2}{16}(A_1 - A_2) - \frac{c'h_1}{4N}(A_2) + \frac{c'h_1}{16N}(A_2 - A_1)$ $D_5 = -\frac{Tx_5^2}{16}(3A_4 + A_3) + \frac{Th_1 x_5}{8}(-A_4 + A_3 - A_2 - A_1) + \frac{Th_1^2}{16}(A_4 - A_3 + A_2 - A_1) + \frac{c'x_5}{8N}(A_1 + A_2) - x_5 - h_1 + \frac{c'h_1}{16N}(A_1 - A_2)$ $N = \frac{c'(A_1 + A_2)}{4\left[2 + \frac{Tx_5}{4}(A_4 + A_3) - \frac{Th_1}{4}(A_4 + A_3 - A_2 - A_1)\right]}$	$B_1 = B_2 = -1;\ B_3 = \frac{Th_1}{6}(A_2 - A_1) + \frac{c'}{6N}(A_1 - A_2) - 1$ $B_4 = \frac{Th_1}{6}(2A_3 - A_2 - A_1) + \frac{c'}{6N}(A_2 - 2A_3 + A_1) - 1$ $B_5 = \frac{Th_1}{6}(3A_4 - A_3 - A_2 - A_1) + \frac{c'}{6N}(A_3 + A_2 + A_1) - 1$ $B_6 = \frac{T}{2}\left(h_1 + \frac{x_7 - h_1}{3}\right)(A_5 - A_4) + \frac{Th_1}{6}(3A_4 - A_3 - A_2 - A_1) + \frac{c'}{6N}(A_3 + A_2 + A_1) - 1$; $B_7 = 1 + \frac{TA_6 x_7}{2}$, $D_1 = D_2 = 0;\ D_3 = -\frac{Th_1^2}{36}(A_2 - A_1) - \frac{c'h_1}{36N}(A_1 - A_2)$ $D_4 = \frac{Th_1^2}{36}(-4A_3 + 3A_2 + A_1) + \frac{c'h_1}{36N}(4A_3 - 3A_2 - A_1)$ $D_5 = \frac{Th_1^2}{36}(-9A_4 + 5A_3 + 3A_2 + A_1) + \frac{c'h_1}{36N}(-5A_3 - 3A_2 - A_1)$ $D_6 = -\frac{T}{4}\left(h_1 + \frac{x_7 - h_1}{3}\right)^2(A_5 - A_4) + \frac{Th_1^2}{36}(-9A_4 + 5A_3 + 3A_2 + A_1) + \frac{c'h_1}{36N}(-5A_3 - 3A_2 - A_1)$ $D_7 = -\frac{T}{4}\left(h_1 + \frac{2(x_7 - h_1)}{3}\right)^2(A_6 - A_5) - \frac{T}{4}\left(h_1 + \frac{x_7 - h_1}{3}\right)^2(A_5 - A_4) + \frac{Th_1^2}{36}(-9A_4 + 5A_3 + 3A_2 + A_1) + \frac{c'h_1}{36N}(-5A_3 - 3A_2 - A_1)$ $N = \frac{c'(A_2 + A_3 + A_1)}{6\left[\begin{array}{l} 2 + \frac{TA_6 x_7}{2} - \frac{T}{2}\left(h_1 + \frac{2(x_7 - h_1)}{3}\right)(A_6 - A_5) - \frac{T}{2}\left(h_1 + \frac{x_7 - h_1}{3}\right)^2(A_5 - A_4) \\ -\frac{Th_1}{6}(3A_4 - A_3 - A_2 - A_1) \end{array}\right]}$

Table 6.5 The generalized expression of B_i's and D_i's for any arbitrary slicing of Regions II and III.

<table>
<tr><td colspan="2">m number of slices in Region II and r number of slices in Region III</td></tr>
<tr><td>Expression of B_i's</td><td>Expression of D_i's</td></tr>
<tr><td>$B_1 = B_2 = -1$
For i= 3 to m+1,
$B_i = \frac{Th_1}{2m}\left[(i-2)A_{i-1} - \sum_{j=2}^{i-1} A_{j-1}\right] + \frac{c'}{2mN}\left[\sum_{j=2}^{i-1} A_{j-1} - (i-2)A_{i-1}\right] - 1$
For i= m+2,
$B_i = \frac{Th_1}{2m}\left[mA_{m+1} - \sum_{j=2}^{m+1} A_{j-1}\right] + \frac{c'}{2mN}\left[\sum_{j=2}^{m+1} A_{j-1}\right] - 1$
For i= $m+3$ to $m+r$
$B_i = \frac{T}{2}\left[h_1 + k\frac{x_{end} - h_1}{r}\right] \times (A_{i-1} - A_{i-2}) + B_{i-1}$ ($k = 1,.....,r\text{-}2$)
For i= m+r+1:
$B_i = 1 + \frac{TA_{m+r}}{2} x_{end}$</td><td>$D_1 = D_2 = 0$
For i= 3 to m+1:
$D_i = \frac{Th_1^2}{4m^2}\left[-(i-2)^2 A_{i-1} + \sum_{j=1}^{i-2}(2j-1)A_j\right] + \frac{c'h_1}{4m^2N}\left[(i-2)^2 A_{i-1} - \sum_{j=1}^{i-2}(2j-1)A_j\right]$
For i= m+2:
$D_{m+2} = \frac{Th_1^2}{4m^2}\left[-m^2 A_{m+1} + \sum_{j=1}^{m}(2j-1)A_j\right] - \frac{c'h_1}{4m^2N}\left[\sum_{j=1}^{m}(2j-1)A_j\right]$
For i= $m+3$ to $m+r$:
$D_i = -\frac{T}{4}\left[h_1 + k\frac{x_{end} - h_1}{r}\right]^2 \times (A_{i-1} - A_{i-2}) + D_{i-1}$
($k = 1,.....,r\text{-}2$)
For i= m+r+1:
$D_i = -\frac{T}{4}\left[h_1 + \frac{(r-1)\times(x_{end} - h_1)}{r}\right]^2 \times (A_{m+r} - A_{m+r-1}) + D_{m+r}$</td></tr>
<tr><td colspan="2">$$N = \frac{c'\sum_{j=1}^{m} A_j}{2m\left[2 + \frac{TA_{m+r}x_{end}}{2} - \frac{T}{2}\left\{h_1 + \frac{(r-1)\times(x_{end} - h_1)}{r}\right\}\times(A_{m+r} - A_{m+r-1}) - \frac{T}{2}\left\{h_1 + \frac{(r-2)\times(x_{end} - h_1)}{r}\right\}\times(A_{m+r-1} - A_{m+r-2}) - \frac{Th_1}{2m}\left(mA_{m+1} - \sum_{j=2}^{m+1} A_{j-1}\right)\right]}$$</td></tr>
<tr><td colspan="2">N.B.: Here, (i) $T = \gamma \tan\phi'$, (ii) $A_i = 1/(c' - \sigma^s_{avg,i} \tan\phi')$ (iii) $r \geq 3$</td></tr>
</table>

$$\sqrt{\sum_{i=1}^{m+r}\left(y_i^{\substack{current\\iteration}} - y_i^{\substack{previous\\iteration}}\right)^2} < 10^{-5}, \tag{6.23a}$$

$$\left|F_s^{\substack{current\\iteration}} - F_s^{\substack{previous\\iteration}}\right| < 10^{-3}, \text{ and} \tag{6.23b}$$

$$\left|N^{\substack{current\\iteration}} - N^{\substack{previous\\iteration}}\right| < 10^{-3} \tag{6.23c}$$

If the stopping criteria are satisfied, the F_s value and the stability number obtained from the current iteration is reported as the solution to the chosen soil slope subjected to the specified climatic condition. The flow chart, presented in Fig. 6.9, demonstrate the schematic representation of the procedure.

6.5 RESULTS AND DISCUSSIONS

Following the iterative technique, some typical homogeneous unsaturated soil slopes are analysed by varying the following parameters:

Slope geometry: (i) Slope angle (β = 30^o to 90^o at an interval of 5^o)

(ii) Height of slope (h =1 to 10 m at 3m interval)

Material parameters: (i) Cohesion: c' = 10 kPa

(ii) Saturated hydraulic conductivity: k_s = 5 x 10^{-8} m/s

(iii) Angle of internal friction: ϕ = 15^o to 40^o at 5^o interval

(iv) Air-entry pressure: α^{-1} = 10 to 100 kPa at 10 kPa interval

(v) Pore spectrum number: n = 1.1, 2.0, 2.5, 4.0, 8.5

(vi) m and n relationship: R_M =0, 2

(vii) θ_s= 0.58, θ_r= 0.05 (GD SWCC for Transient analysis)

Flow conditions: (i) No flow (Hydrostatic, i.e. q = 0)

(ii) Steady-state Infiltration: a) q = -3.14 x 10^{-8} m/s or

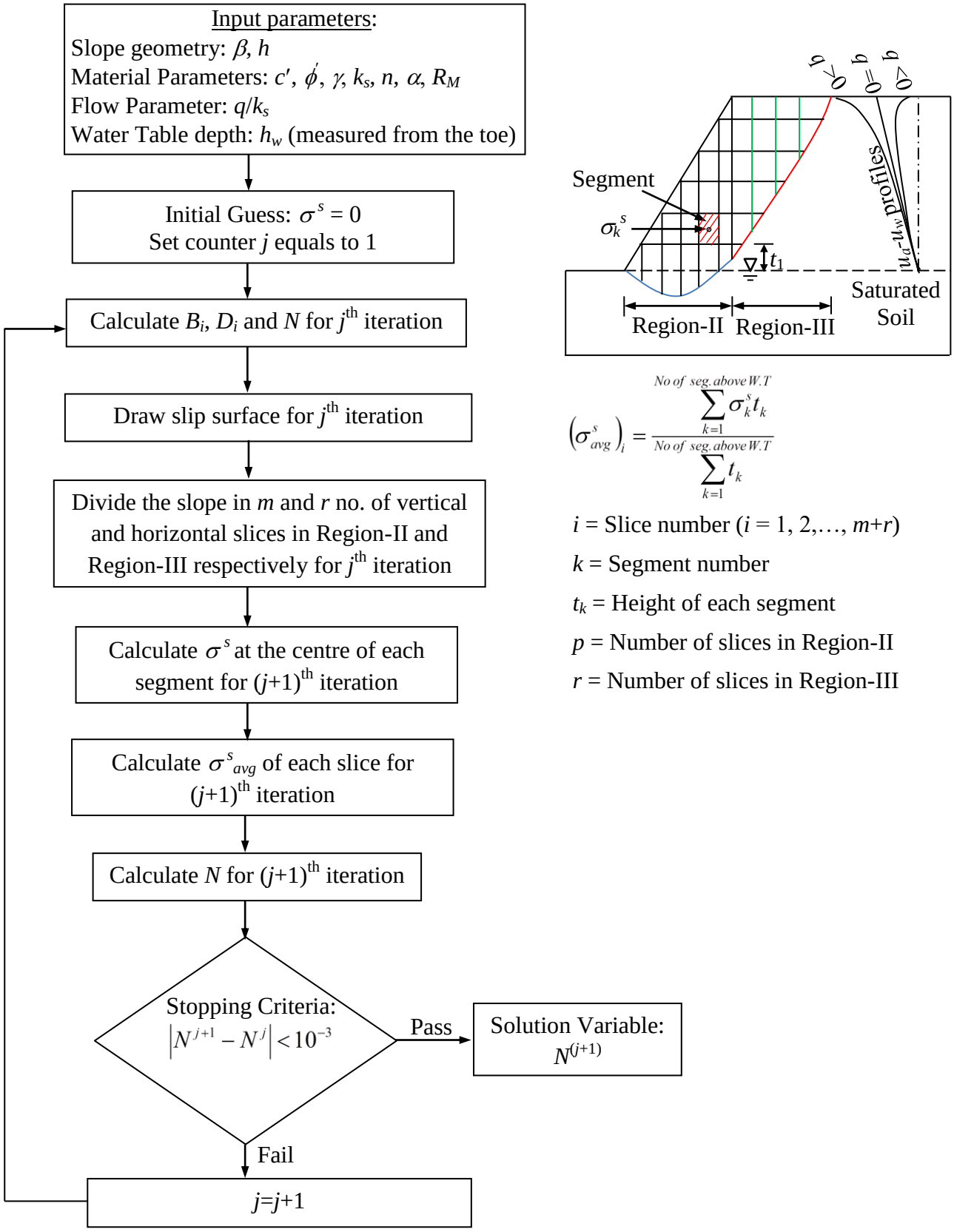

Fig. 6.9 Flowchart for the present iteration technique.

b) q/k_s =–0.2, –0.4, –0.6, –0.8, –1

(iii) Steady-state Evaporation: a) q = 1.15 x 10^{-8} m/s

b) q/k_s =0.2, 0.4, 0.6, 0.8

(iv) Transient Infiltration: q/k_s = –0.4, –0.8

Water table depth: h_w (measured from the toe surface) =0 to 4m at an interval of 1m

These input parameters are selected through a rigorous literature study (Lu and Likos 2004; Vahedifard et al. 2016; Sun et al. 2019; Shahrokhabadi et al. 2019; Gu et al. 2020) so that a wide possible range of various combination of parameters in the field gets considered.

6.5.1 Influence of slope geometry (β and h)

Fig. 6.10 depicts the combined impact of slope angle and slope height on the magnitude of stability number. For the same soils with constant water table, higher the value of β and h, higher is the N value. It is to be noted that increment in N apparently indicate in worsening the safety factor. The stability curves with respect to β appears to be either concave upwards (for low h, say h=1) or convex upwards (for high h, say h=10). Two noteworthy observations for the slopes with high h are the following: (a) the rate of increment in N decreases with the increasing steepness of the slope, and (b) the deviation between the stability curves generated from the hydrostatic and the steady state flows remains almost to be constant and thus irrespective of the flow conditions, the stability curves with respect to β appears almost parallel to each other. However, this observation is not true for the shallow slopes. As an example, when β varies from 30^o to 90^o, corresponding to evaporation, hydrostatic, and percolation, the magnitude of

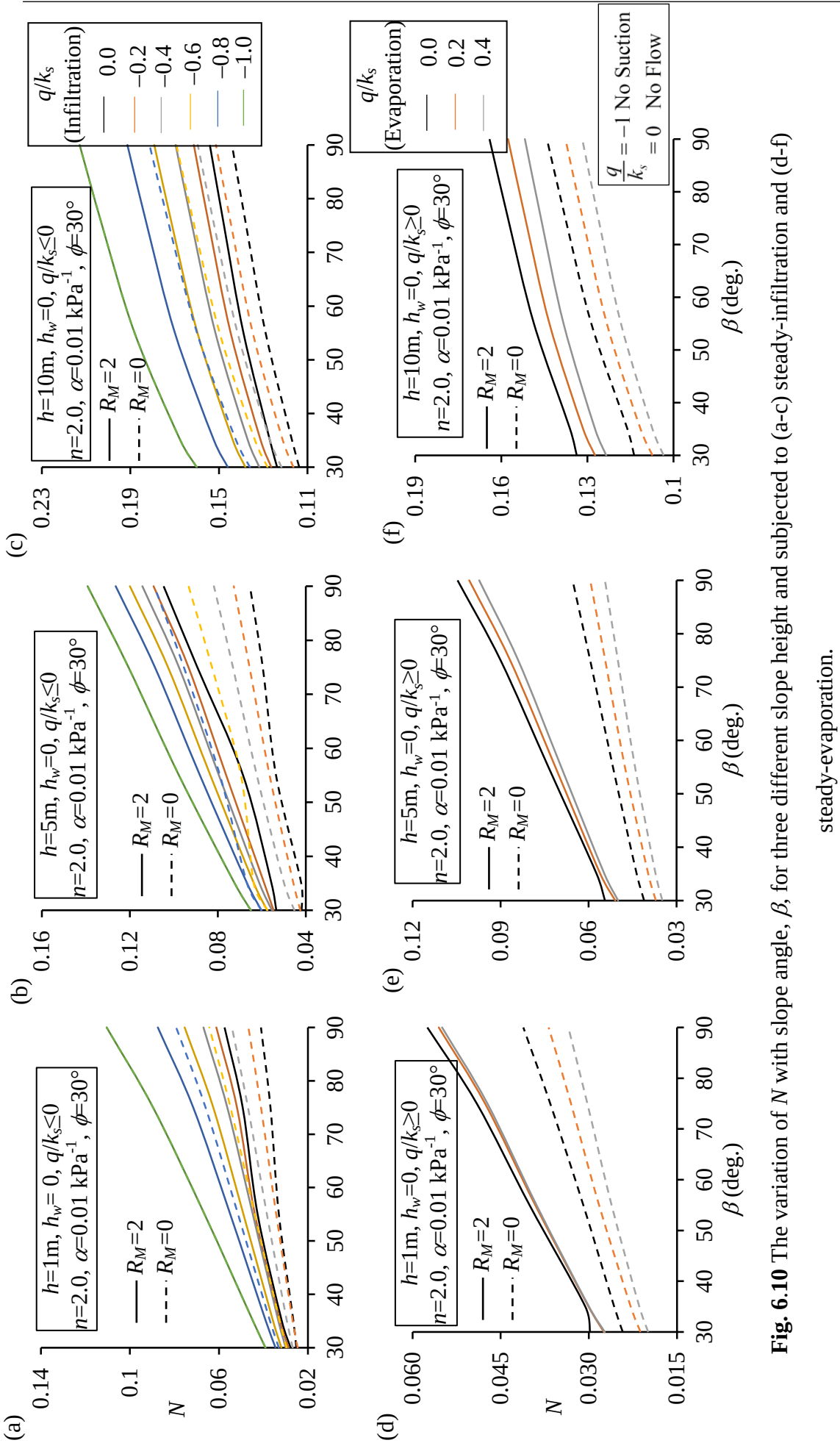

Fig. 6.10 The variation of N with slope angle, β, for three different slope height and subjected to (a-c) steady-infiltration and (d-f) steady-evaporation.

N increases by (i) 60.86%, 62.32%, and 66.39%, respectively for a 1m slope and (ii) 34.28%, 34.81%, and 35.05%, respectively for a 10 m slope.

Fig. 6.11 indicate the nonlinear variation in *N* value by elevating the slope height and by maintaining the slope angle at a specific value (β=35^o). The parallelism of the curves suggests that the difference in the *N* value between two slopes of contrasting height does not depend on the soil's frictional strength. Irrespective of α and *m* parameters, the deviation of the *N* value emerges quite significantly when the height is altered for the slopes with high *h* rather than the slopes with low *h*. For an example, corresponding to a specific soil (say, ϕ=30^o, α=0.1kPa^{-1}, R_M= 0) the percentage increment in *N* value is remarkably visible when the slope height is increased from 7 to 10m (almost 98%) but the variation is not so significant when the slope height changes from 1 to 4m (nearly 25%).

6.5.2 Influence of material parameters *(ϕ, 1/α, n, and m)*

Fig. 6.11 illustrates the reduction pattern of *N* with the enhancement of frictional strength parameter. The rate of decrement of *N* is higher for the relatively weaker soils. Irrespective of the slope height, percentage improvement of safety functional, with the increase in ϕ, remains almost the same. The influence of air entry value and the pore size distribution on the stability of soil slope is depicted in Fig. 6.12. This figure pertains to 60^o slope with ϕ = 30^o and represents the solutions for $q \geq 0$. It can be inferred from the figure that there is an abrupt fall in the stability number upto a certain α^{-1} beyond which the value of *N* remains almost constant and unaltered by the pore matrix. It appears that if the magnitude of AEV is greater than 50kPa, there is almost insignificant influence on the stability of soil slopes.

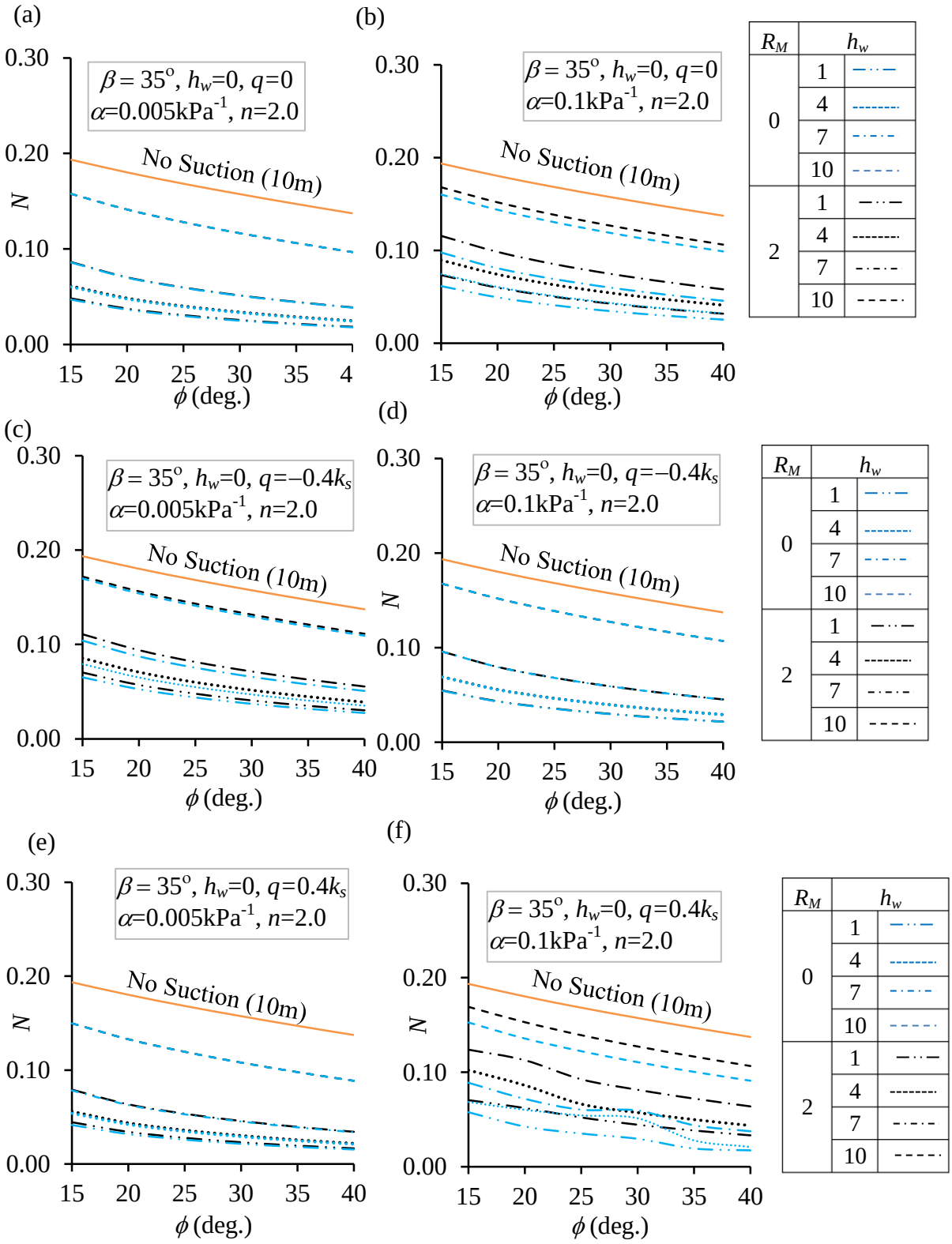

Fig. 6.11 The variation of N with frictional strength for two different R_M and three different steady-state flow, namely, (a, b) no flow (q=0); (c, d) infiltration (q=–0.4k_s); and (e, f) evaporation (q=0.4k_s).

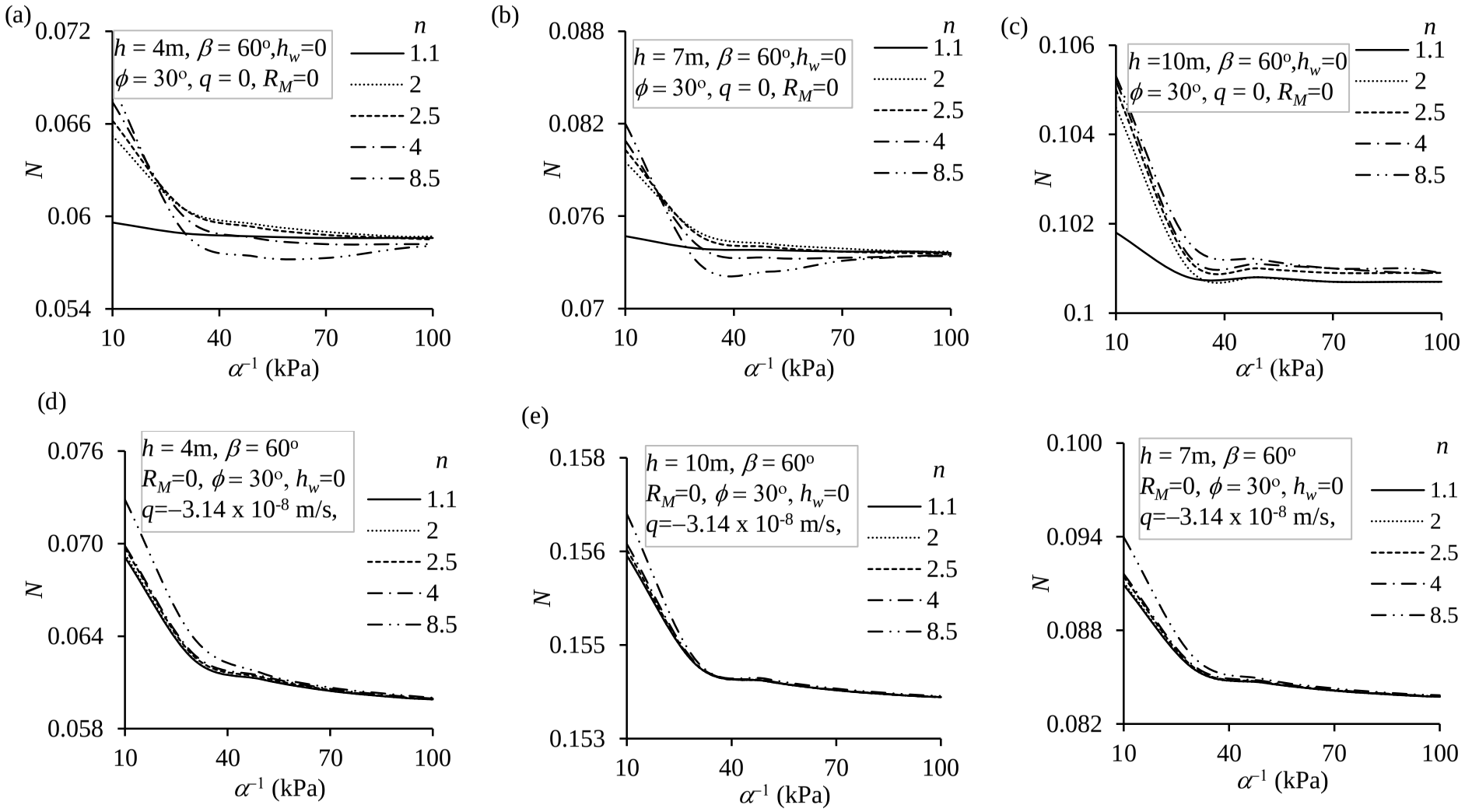

Fig. 6.12 The variation of N with the inverse of α corresponding to three different slope height h, namely, 4m, 7m, and 10m and subjected to (a-c) no flow (q = 0) and (d-f) steady-state infiltration (q =–3.14 x 10^{-8} m/s).

The impact of AEV, below 50 kPa, further gets influenced by the height of the slope. For an illustration, corresponding to β = 60^o and n = 8.5, when α^{-1} increases from 10 to 50 kPa the magnitude of N reduces by 15.18% and 4.18% for slope height (h) equals to 4m and 10m, respectively. Fig. 6.13 further shows the variation of N with respect to the AEV corresponding to 45^o slope and three flow conditions. For hydrostatic condition, a notable change in stability is observed when n rises from 1.1 to 2.5 but surprisingly there is no appreciable variation in N value for any further increment of n. The impact of the n value on the stability curve appears to be more pronounced for evaporative condition. It can be concluded from this discussion that the stability of cohesive-frictional homogenous soil slope, especially for less height, would get affected if AEV and n do not exceed 50kPa and 2.5, respectively.

In addition to that, Figs. 6.10, 6.11, and 6.13 also represent an important aspect of the m and n relationship. Two different relationships are being used for this verification, namely, R_M=0 ($mn+1=n$) and R_M=2 ($mn+1=3n$). Higher the R_M lower is the factor of safety. This can be attributed to the fact that with the increase in R_M, suction stress decreases to a great extent and eventually resulting in lower estimation of effective stress and higher prediction of the stability number. It can be interpreted that higher R_M always provides conservative solution. Unlike R_M=0, the discrepancy in the stability curves arises due to the rise in evaporation rate is inappreciable for R_M=2, especially, for low-height slopes (Fig. 6.10d-6.10e). It can be further inferred from Fig. 6.11 that for soils with very high AEV the influence of R_M on the stability values is insignificant. On the contrary, the deviation of the stability curves emerge from various soil pore configuration becomes wider for higher values of R_M. This discussion suggests that instead of incorporating the traditional relationship between m and n, it is advisable

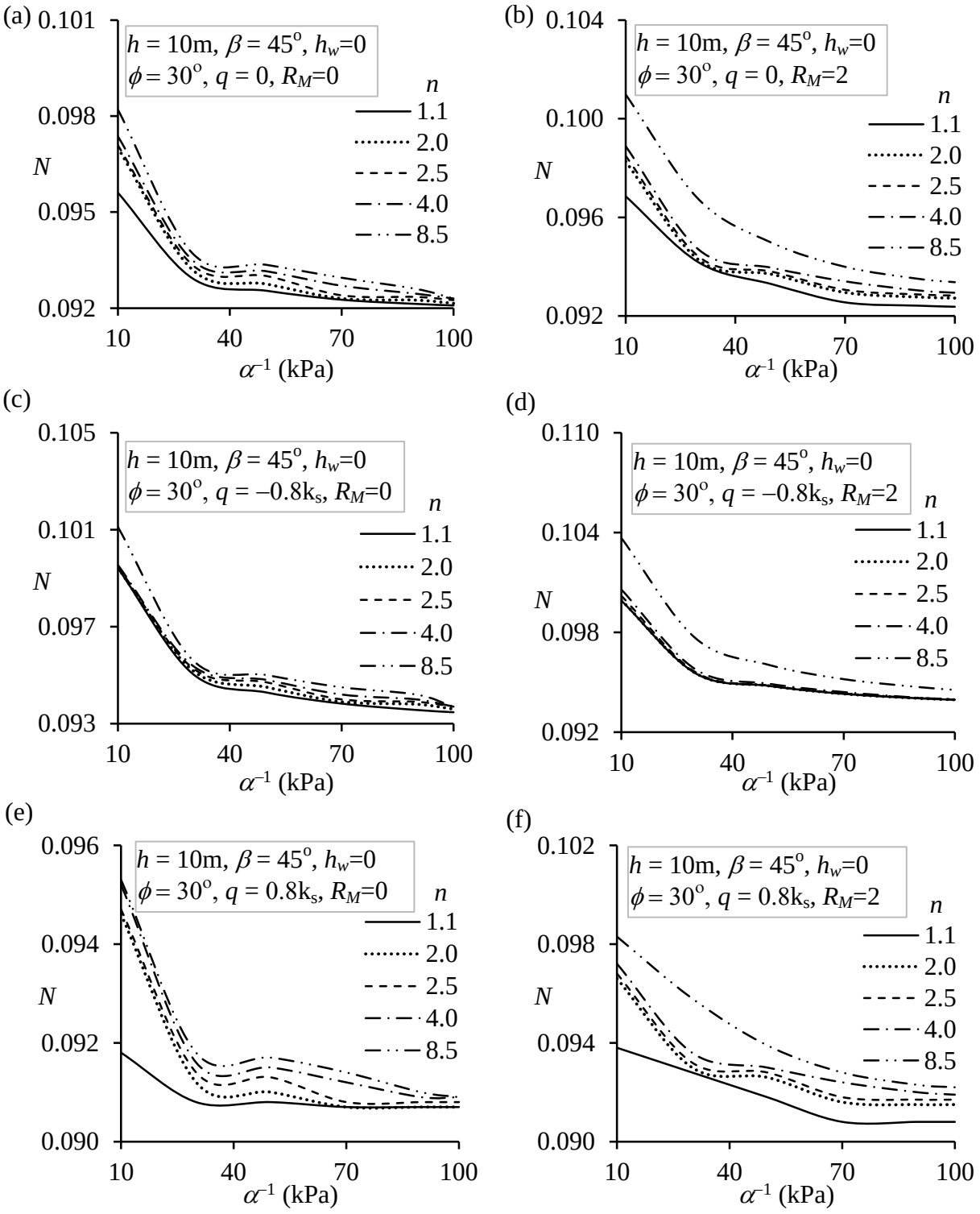

Fig. 6.13 The variation of N with α^{-1} corresponding to two R_M's and subjected to: (a, b) no flow condition (q = 0), (c, d) steady-infiltration ($q = -0.8k_s$) and (e, f) steady-evaporation ($q = 0.8k_s$).

to deduce the *m* value independent of *n* and use the correct form of *m* in the stability analysis.

6.5.3 Influence of flow conditions and water table position

The flow conditions further impact the stability of unsaturated soil slopes. Fig. 6.10 clearly gives an impression that for a certain soil slope, stability number corresponding to infiltration is the maximum and this is followed by no-flow condition and then follows by the solutions generated from evaporative condition. Fig. 6.11 depicts that when suction stress is not incorporated in the analysis, the flow condition not at all influence the stability curve profiles. It can be further interpreted from Fig. 6.12 that as water percolates from the ground surface, no matter whatever be the gradation of the soil, the deviation of the stability curves generated from various *n* values become less. With the increase in slope height, this deviation of the stability value corresponding to poorly and well graded soil also reduces. Furthermore, the variation of stability number with respect to different α and *n* values are depicted in Fig. 6.13 corresponding to β=45^{o} slope and three values of q/k_s, namely, 0, –0.8, and 0.8. It is inferred that irrespective of slope geometry, the variation of the stability curves due to the soil gradation remains more appreciable during the drying of soil. With the increase in infiltration rate, the difference in the stability number corresponding to low (10 kPa) and high (100 kPa) AEV reduces to a noticeable extent. This reduction becomes further discernible as the slope height and slope angle increase.

Figs. 6.14a and 6.14b present the variations of stability number with the soil frictional strength subjected to the steady and transient flow of water; Fig. 6.14a pertains to *h* = 1m and Fig. 6.14b corresponds to *h* = 10m. For transient flow, the stability curves are drawn at four different time periods, namely, 10, 100, 200, 400, and 1000 days. After a small duration of transient flow, the σ^s is significantly higher than its steady-state counterpart; therefore, the deviation between the stability curves obtained from the steady flow and the transient flow

with small t, is appreciably high. With the advancement of time, the stability curves for transient flow approach towards the steady-state profile and hence, the stability curves pertaining to the steady-state flows always remain above the transient curves, irrespective of slope geometry and soil strength. Figs. 6.14c and 6.14d further present the stability profiles with respect to the elapsed time. The curves are plotted for three different values of α, namely, 0.005, 0.01, and 0.02 kPa^{-1}. For the chosen time period, the stability profile for various α remains to be distinctive while h = 4m; however, for h = 10m, the α parameter impacts the stability at the initial days of transient flow, thereafter, the curves turn into a horizontal plateau and coincide with the steady state profiles.

By fluctuating the water table position, Fig. 6.15 shows the variation of N corresponding to three different slope angles (β =45^o, 60^o, 75^o) and subjected to various steady-flow conditions. The magnitude of N is minimum when the water table lies at the toe surface. As the water table rises, the N value steadily increases up to a certain position, thereafter; any further inflation of the water table surface does not impact the N value. This can be inferred that as far as stability number is concerned, alteration of the water table near the slope toe is more impactful than the fluctuations of the water table adjacent to the ground surface.

Additionally, this variation of the water table near the slope toe manifests its further effect on the steeper slope, experiencing an upward flow of water. For example, when the water table inflates by 4m from the toe surface, the factor of safety corresponding to β=60^o and h=7m decreases by 11.60%, 26.12%, and 29.83% for infiltration, no flow condition, and evaporation, respectively. For the same upliftment of the water table in a 75^o soil slope, this reduction is reported to be 15.70%, 32.60%, and 37.90% corresponding to the three steady-flow condition.

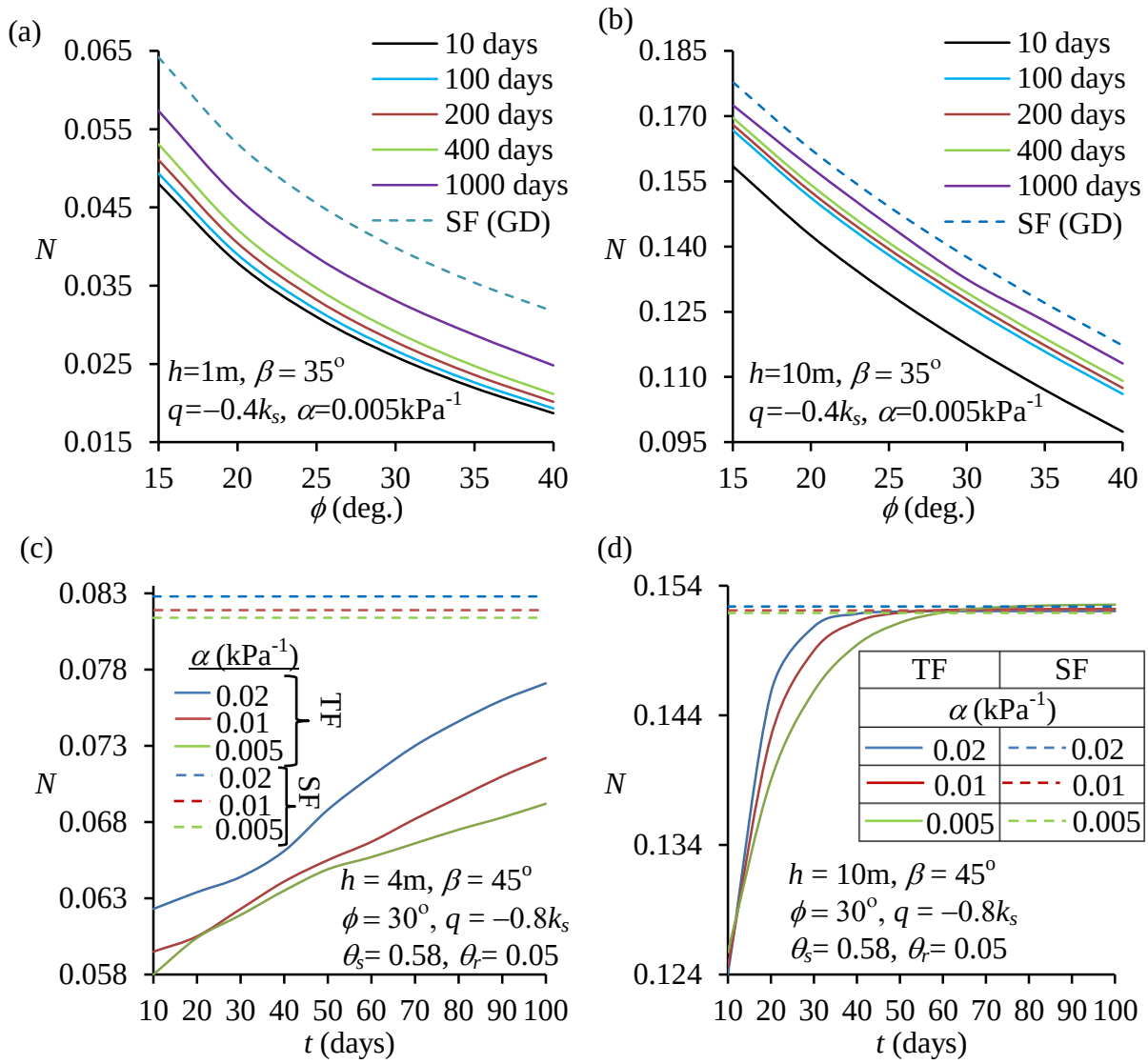

Fig. 6.14 The variation of *N*, corresponds to steady-state and transient flow, with respect to the (a-b) soil friction angle, and (c-d) time.

6.5.4 Failure patterns

Fig. 6.16 depicts the influence of slope angle, frictional strength, and AEV on the form of the critical failure surface. The process of the development of slip surfaces through the iterative techniques are clearly displayed in the figure. It gives a clear impression that the encompassed area within the failure surface grows in size as the suction stress is incorporated in the analysis. Comparing Figs. 6.16a and 6.16b, it can be seen that as the slope angle increases, the volume covered by the failure surface reduces to a great extent. It can be interpreted that smaller amount of soil is required to mobilize before the occurrence of slope

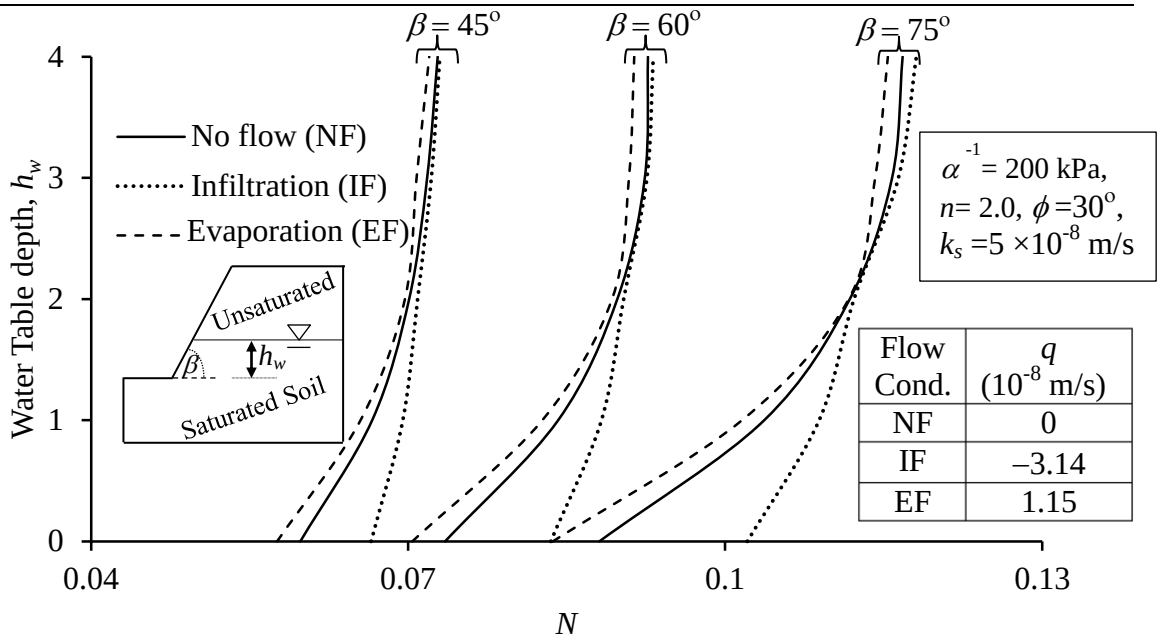

Fig. 6.15 The variation of N with respect to the water-table position pertaining to three slopes (β = 45°, 60°, 75°) and three steady-state flows (q=0, –3.14×10^{-8}m/s, 1.15×10^{-8} m/s).

failure in steep slopes. Figs. 6.16a and 6.16c depict the form of the failure surface for ϕ equals to 30° and 40°, respectively. For stronger soil slopes, higher number of iterations are required to achieve the critical state, and the volume of the soil involved in the failure zone expands. However, for the same frictional strength, the smaller the AEV lesser is the horizontal extent of the failure surface on the ground surface. In other words, it can be inferred that the failure surface encompasses less volume of soil corresponding to smaller AEVs.

Fig. 6.17 shows the impact of climatic conditions and the R_M parameter on the size and shape of the critical failure surface. The figures are drawn for β=55°, α=0.01, ϕ=40° and subjected to three flow conditions and two R_M values, namely, R_M =0 and R_M =2. The figure reveals that the horizontal and the vertical extent of the failure zone are maximum for the evaporation and least for the infiltration condition. The zone of failure surface further reduces with the increase in R_M parameter.

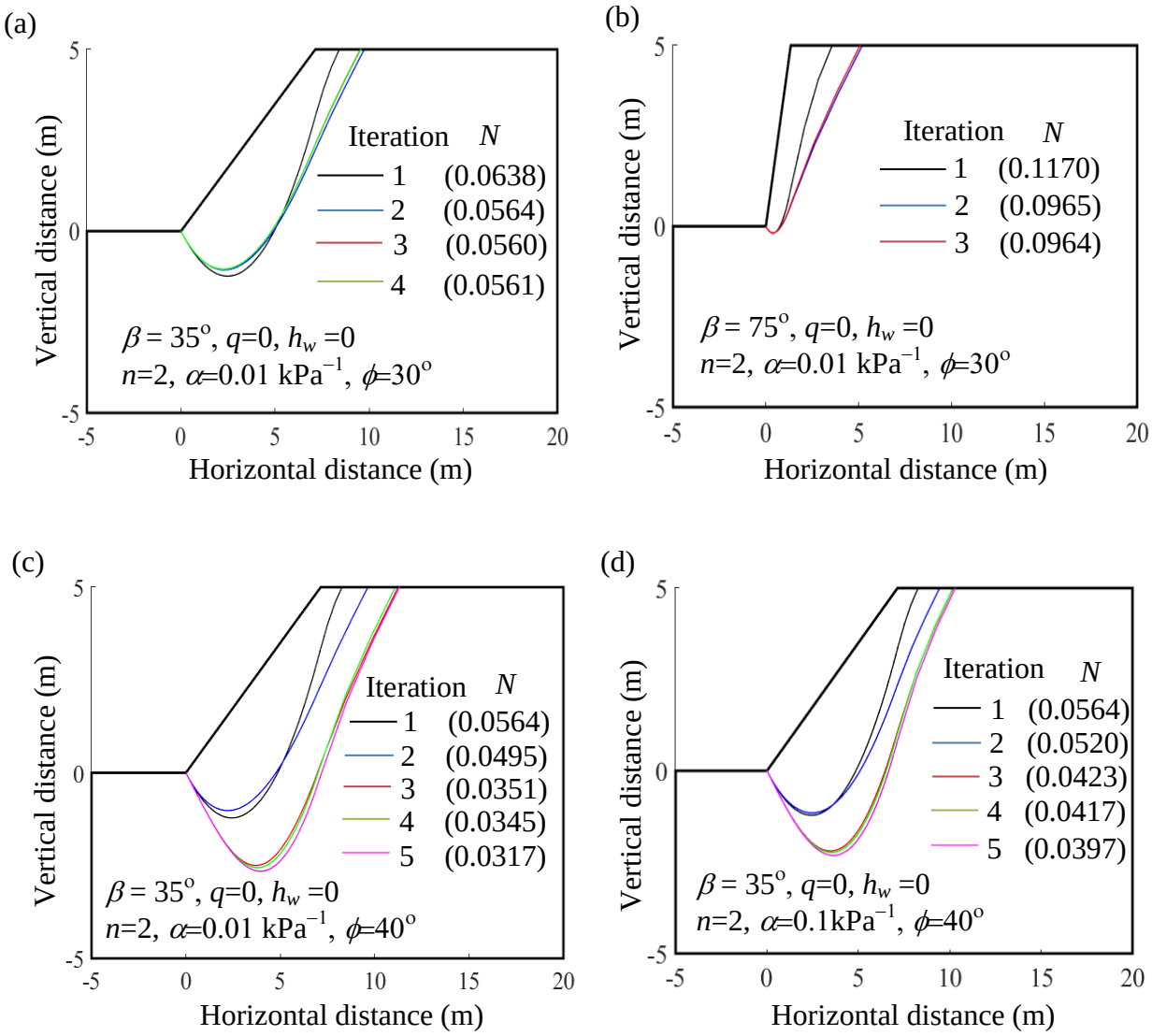

Fig. 6.16 The evolution of critical failure surface through the numerical iteration corresponding to unsaturated soil slopes having (a)β =35°, α=0.01 kPa^{-1}, ϕ=30° ; (b) β =75°, α=0.01 kPa^{-1},ϕ=30°; (c) β =35°, α=0.01 kPa^{-1},ϕ=40°; (d)β=35°, α=0.1 kPa^{-1}, ϕ=40°.

Fig. 6.18 presents the development of the critical failure surface during transient flow of water corresponding to β=55°,α=0.01 kPa^{-1}, ϕ=40° and q/k_s = –0.8. The slip surfaces are obtained at three specific time duration, i.e., 10, 100, and 400 days. It is observed that the number of iterations for obtaining the failure state is higher for transient analysis and with the advancement of time; the size of the failure zone diminishes.

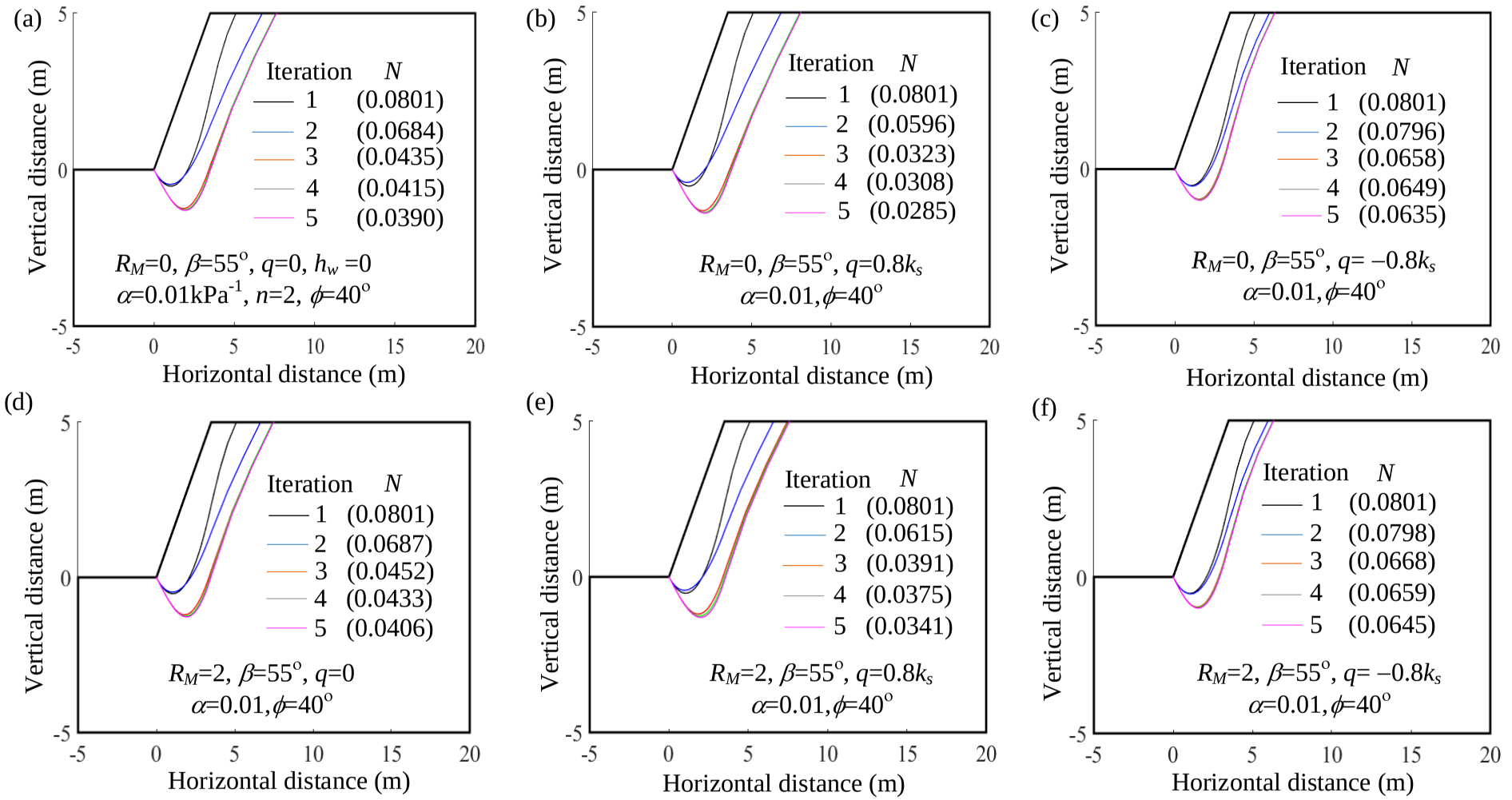

Fig. 6.17 The evolution of critical failure surface for two different m and n relationships (a, b, c) R_M=0 and (d, e, f) R_M=2 and subjected to three steady-state flows: (a,d) q=0, (b,e) q=0.8k_s, and (c,f) q=–0.8k_s.

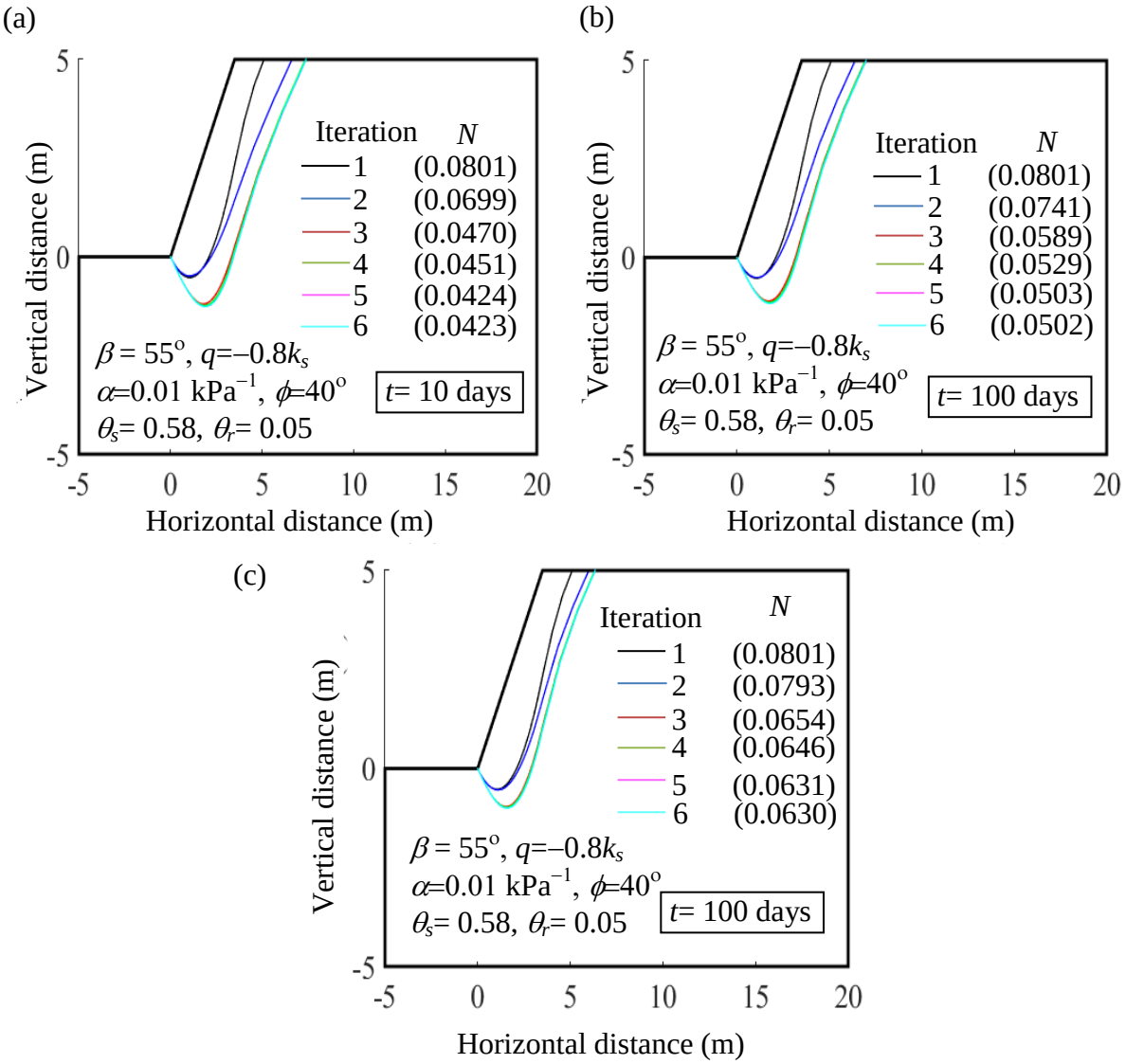

Fig. 6.18 The evolution of critical failure surface for transient flow corresponding to *t* equals to: (a) 10 days, (b) 100 days, and (c) 400 days.

6.6 COMPARISONS OF RESULTS

Table 6.6 illustrates the comparison between the present solutions and available results presented by Vahedifard et al. (2016) and Sun et al. (2019). It is observed that the magnitude of *N* in the present analysis is higher than Vahedifard et al. (2016)'s and Sun et al. (2019)'s solutions. In other words, it can be reiterated that the factor of safety from the present analysis is smaller than the available reported values. It indicates the conservatism in the present solutions. It is noteworthy that Vahedifard et al. (2016) and Sun et al. (2019)

employed limit equilibrium and upper bound rigid block method for analysing the unsaturated slope stability problem, respectively. Vahedifard et al. (2016) assumed that the shape of the failure surface is log-spiral and Sun et al. (2019) considered log spiral mechanism in the analysis. The present variational technique is statically determinate and there is absolutely no requirement to pre-assume either the shape of the failure surface or the failure mechanism prior to the analysis.

Table 6.6 A comparison of the present computed stability number (N) with the solutions presented by Vahedifard et al. (2016) and Sun et al. (2019)

		β= 90°, n=2, α^{-1}=200kPa, h_w=0, q=0, R_M=0		
h (m)	ϕ' (°)	Present Study	Vahedifard et al. (2016)	Sun et al. (2019)
1	15	0.1677	0.1397	0.1347
	20	0.1541	0.1016	0.0989
	25	0.1427	0.0619	0.0608
	30	0.1326	0.0227	0.0215
	35	0.1235	0.0014	0.0017
4	15	0.2155	0.1425	0.1370
	20	0.2071	0.1032	0.0954
	25	0.1994	0.0631	0.0577
	30	0.1921	0.0239	0.0204
	35	0.1850	0.0017	0.0016

Corresponding to different slope geometry and flow conditions, Table 6.7 shows the comparison of present results with the solution provided by Gu et al. (2020) on the basis of upper bound rigid block method considering rotational failure mechanism (log-spiral). Following Gu et al. (2020), the parameters that are considered in this comparison are h = 5m, α = 0.005 kPa^{-1}, n = 2 and unit weight of soil (γ) = 20 kN/m^3. Due to the upper bound nature of Gu et al. (2020)'s solution, the present safety factor appears to be on the lower side of the solutions than that of Gu et al. (2020), nevertheless, the solution trend matches quite well.

Table 6.7 A comparison of the present solutions with the results reported by Gu et al. (2020) corresponding to different slope angle (β) and subjected to various steady-flow conditions.

	h = 5m, h_w=0, n=2, α=0.005kPa^{-1}, k_s =5 x10^{-8} m/s, ϕ = 30^{o}, R_M =0		
β	Infiltration (q = –3.14×10^{-8}m/s)	No flow/ Hydrostatic (q = 0m/s)	Evaporation (q = 1.15×10^{-8}m/s)
45^{o}	0.1064* (0.0398)	0.0984 (0.0150)	0.0956 (––)
60^{o}	0.1241 (0.0620)	0.1145 (0.0250)	0.1103 (0.2000)
75^{o}	0.1408 (0.1240)	0.1284 (0.0700)	0.1239 (0.0350)
90^{o}	0.1586 (0.1524)	0.1439 (0.1009)	0.1385 (0.0816)

***N.B.:** The values mentioned within and outside the parenthesis denote the stability number computed from the present variational analysis and Gu et al. (2020)'s upper bound rigid block analysis, respectively.

6.7 SUMMARY

This chapter proposes a novel methodology for determining the closed form critical factor of safety for unsaturated homogeneous soil slopes. The approach utilizes variational techniques, which is the first of its kind for solving unsaturated soil slope problems. The unified suction-stress-based effective stress formulation is explicitly employed to simulate the problem, effectively capturing the spatial flow of water induced by climate change. A comprehensive parametric study is performed to investigate the influence of various factors on slope stability. The concerned parameters considered include slope geometry, unsaturated soil properties, soil strength, water flow behaviour, and water table position. The solutions

are presented in terms of stability numbers, and insightful observations are made regarding the stress changes in the vadose zone. To validate the proposed methodology, the computed solutions are compared with results from the previous literature. The comparison demonstrates the effectiveness and accuracy of the new approach. The design charts derived from this study provide valuable guidance to practicing engineers in assessing the stability of homogeneous unsaturated soil slopes under both steady-state and transient flow conditions.

6.8 LIMITATIONS

The present study focuses on formulating slope stability analyses without considering stress–strain and strain–displacement relationships. The formulations exclusively rely on strength parameters, attributing soil failure to the modified Mohr-Coulomb yield criterion (MMC). Furthermore, the variation of suction stress in the unsaturated portion is addressed using the soil-water characteristic curve (SWCC), specifically van-Genuchten's SWCC (vG-SWCC), Gardner's SWCC (Gd-SWCC), and the suction stress characteristics curve (SSCC). It is acknowledged that using different SWCC models could yield different results. Additionally, the slope is assumed to be homogeneous, single-stage, with a constant factor of safety along the entire slip surface, though recognizing that for high slopes, considering multiple stages may provide more realistic stability values. Moreover, the stability charts presented are applicable within specified parameter ranges, and if field conditions extend beyond, determining the critical factor of safety is easily achievable using the provided formulations.